Spatially resolved single atom detection of neutral atoms

by

Kirsten Viering

Thesis

Presented to the Faculty of the Graduate School of

The University of Texas at Austin

in Partial Fulfillment

of the Requirements

for the Degree of

Master of Arts

The University of Texas at Austin

August 2006

Spatially resolved single atom detection of neutral atoms

Approved by
Supervising Committee:

_____

_____

Für meine Eltern

Acknowledgments

First of all I would like to thank my supervisor, Mark Raizen. His enthusiasm for physics and his willingness to share his new ideas with his students is exceptional and contribute greatly to the pleasant atmosphere in his lab. I am glad he gave me the opportunity to work in his group.

The great atmosphere is also due to the pleasant people in the lab. I especially wish to thank my fellow Sodium group members, Kevin, Hrishi, and Tongcang. Kevin and Hrishi had infinite patience in answering all of my questions and were always willing to show me new things. All of them spent a huge amount of time helping me with "my" experiment and calculations and their good moods eased my frustrations.

Another person who always seems to be in a good mood is Ed, our postdoc. I appreciate his way of answering questions and his making my questions a priority even though I was not working on the same experiment. His view on quantum mechanics and his explanations taught me a lot of things.

I was also glad to share the office with Adam and Max, both of them good friends with whom I also spent most of my spare time. I truly enjoyed our discussions about physics and life in general. Thanks for all the fun we had inside and outside the lab.

Thanks also to the rest of the lab members, Gabe, Chih-Sung, and Isaac. They added tons of little things to the daily life in the lab that made my stay in Texas and particularly on the second floor so enjoyable.

I am grateful that Prof. Böhm, Prof. Langhoff, and Prof. Fink are keeping the Würzburg program alive and thus making it possible for Würzburg students to come

here every year. Thanks also to my family for all their support and to everybody who made Austin such a lovely place to stay.

Thanks to everybody who helped reading and correcting my thesis.

I would also like to acknowledge the German Academic Exchange Service (Deutscher Akademischer Austausch Dienst) for their financial support.

Kirsten Viering

The University of Texas at Austin
August 2006

Spatially resolved single atom detection of neutral atoms

Kirsten Viering, M.A.
The University of Texas at Austin, 2006

Supervisor: Mark Raizen

This thesis describes several new ideas towards spatially resolved single atom detection, using a magic wavelength and spatially resolved stimulated Raman transitions.

After an introduction to the theory of AC-Stark shifts and the magic wavelength, we will present the calculations on the magic wavelength for Sodium and Rubidium. We conclude the first chapters by summarizing the experimental efforts made in order to determine the magic wavelength in Sodium.

The theory for stimulated Raman transitions will be described in chapter 5 and evaluated in chapter 6 for Sodium atoms, including a prediction for the ideal pulse area and the spatial resolution achievable using magnetic field gradients.

Contents

List of Figures

Chapter 1

Introduction

In the last few decades, the experimental study of the interaction of electro-magnetic radiation with "cold" atoms has led to a new field of research, *Atom Optics*. It is possible today to cool atoms as Sodium and Rubidium to only a few millionth of a degree with a laser cooling mechanism. In this region, the wave nature of the atoms becomes apparent and opens up possibilities for the study of interesting atom-light interactions and quantum phenomena.

In 1982 Metcalf et al. showed the first slowing of atoms in an atomic beam [1] and in 1985 Chu et al. succeeded in cooling trapped atoms [2]. The rapid development made in cooling and precise manipulation of atoms finally led to the first Bose Einstein Condensate in 1995 by Cornell and Wieman in Boulder , Colorado [3]; a phenomenon predicted by Albert Einstein in 1925 [4].

In the last ten years many questions have been addressed to BEC-systems, such as the interaction with an optical lattice and the transition between a superfluid and a Mott-insulator [5]. The techniques developed make it possible to think of studying the quantum statistics of atoms, with the hope of observing such phenomena as atom bunching and anti-bunching, comparable to similar phenomena in quantum optics and doing controlled studies of entanglement in an atom number state.

Single atom detection and spatially resolved measurements are needed for these type of studies; a magic wavelength tweezer and spatially resolved Raman transitions

are therefore useful tools. A tweezer at the magic wavelength would allow to trap atoms in the ground state as well as in an excited state without heating them. Thus transitions between these two states can be induced and fluorescence imaging can be used to determine the atom number. Spatially resolved Raman transitions allow to measure spatial distributions where the achievable resolution is smaller than the wavelength.

As this work deals with the manipulation of atomic states with light we will review the semi-classical description of atoms with non-resonant light (chapter 2) and apply it to calculations of the AC-Stark shift in Sodium and Rubidium. Knowing the respective energy shifts for the ground and the excited states we can determine the magic wavelength, where the relative shift between the ground and a specific excited state vanishes (chapter 3). Our efforts to determine the magic wavelength in Sodium are summarized in chapter 4, together with a brief discussion of the experimental environment.

In chapter 5 we expand the theory of the interaction of electro-magnetic radiation with atoms to the case with two monochromatic light sources and introduce stimulated Raman transitions in the presence of an external magnetic field. Chapter 6 summarizes our calculations of stimulated Raman transitions for Sodium atoms, and outlines the spatial resolution that is prospectively achievable using a magnetic field gradient.

A relevant parameter in all our calculations is the dipole matrix element between two states. A convenient way to determine these is the Wigner-Eckart Theorem which is briefly discussed in appendix A. Appendix B summarizes some physical properties of Sodium atoms and describes the influence of an external magnetic field on the energy level structure. The Einstein-coefficients we calculated to determine the magic wavelength in Rubidium are tabulated in appendix C.

Chapter 2

Interaction of atoms with non-resonant light

In this chapter we give a brief introduction into the theory of the interaction of atoms with *non-resonant* light. We restrict the treatment to purely monochromatic light and use a semi-classical expression for the interaction Hamiltonian.

2.1 Time-dependant Schrödinger equation

A dynamical quantum mechanical system is described by the time-dependant Schrödinger-equation

$$H|\Psi(\vec{r},t)\rangle = i\hbar\frac{\partial}{\partial t}|\Psi(\vec{r},t)\rangle. \tag{2.1}$$

For the interaction of atoms with light this equation cannot be solved analytically. Hence we will use perturbation theory and treat the time-dependant electro-magnetic light field as a perturbation [6]. We separate the total Hamiltonian $H(t)$ into two terms, $H(t) = H_0 + H'(t)$, where H_0 is time independant; the explicit time dependance is treated in $H'(t)$ as perturbation to the solution of the stationary Schrödinger-equation.

The solution to the time-independant Schrödinger equation is given by the

eigenfunctions $|n\rangle$ with the corresponding energy eigenvalues $E_n = \hbar\omega_n$, $H_0|n\rangle = E_n|n\rangle$. We will write the time-dependant wavefunction $|\Psi(\vec{r},t)\rangle$ as superposition of eigenstates $|n(\vec{r})\rangle$,

$$|\Psi(\vec{r},t)\rangle = \sum_n c_n(t)e^{-i\omega_n t}|n(\vec{r})\rangle \tag{2.2}$$

with the time-dependant coefficients $c_n(t)$. The Schrödinger equation thus becomes

$$\begin{aligned} H(t)|\Psi(\vec{r},t)\rangle &= (H_0 + H'(t))\sum_n c_n(t)e^{-i\omega_n t}|n(\vec{r})\rangle \\ &= i\hbar\frac{\partial}{\partial t}\sum_n c_n(t)e^{-i\omega_n t}|n(\vec{r})\rangle \end{aligned} \tag{2.3}$$

Eq. 2.3 can be further evaluated by multiplication from the left with $\langle m|$ and integrating over spatial coordinates. This leads to a set of differential equations for the coefficients $c_n(t)$,

$$i\hbar\frac{dc_m(t)}{dt} = \sum_n c_n(t)H'_{mn}(t)e^{i\omega_{mn}t}, \tag{2.4}$$

where $H'_{mn} = \langle m|H'(t)|n\rangle$ and $\omega_{mn} = \omega_m - \omega_n$.

2.2 Interaction of a two-level atom with non-resonant light

Let us consider the case of a periodic perturbation with frequency ω, more precisely an oscillating electric field described by $\vec{E}(\vec{r},t) = \frac{1}{2}\vec{E_0}e^{i(\vec{k}\cdot\vec{r}-\omega_l t)} + c.c.$. In most cases the spatial dependance of the electric field is negligible when considering the interaction of atoms with light, since the extend of the electric field is on the order of λ (a few hundred nanometers) while the atoms are several orders of magnitude smaller (a few Ångström). The formalism presented here is for non-resonant light; the resonant case has to be treated seperately.

We will apply the common dipole approximation for radiative transitions of the atoms [7]. Thus the Hamiltonian becomes

$$H(t) = H_0 - \vec{\mu}\cdot\vec{E}(t), \tag{2.5}$$

with the perturbation $H'(t) = -\vec{\mu}\cdot\vec{E}(t)$. The set of differential equations, eq. 2.4, specifies to

$$\frac{\partial c_m(t)}{\partial t} = \frac{i}{\hbar}\sum_n \vec{\mu}_{mn}\vec{E}(t)c_n(t)e^{i\omega_{mn}t}, \tag{2.6}$$

where μ_{mn} describes the dipole matrix element $\langle m|\vec{\mu}|n\rangle$.

Let us first consider the analytically solvable case of a two-level atom. The more general treatment of a multi-level system will be presented in chapter 2.3. In a two-level atom there are two coupled differential equations

$$\frac{\partial c_g(t)}{\partial t} = \frac{i}{\hbar}\vec{\mu}_{ge}\vec{E}(t)c_e(t)e^{i\omega_a t} \tag{2.7}$$

and

$$\frac{\partial c_e(t)}{\partial t} = \frac{i}{\hbar}\vec{\mu}_{eg}\vec{E}(t)c_g(t)e^{i\omega_a t} \tag{2.8}$$

with the resonant absorption frequency $\omega_a = \omega_e - \omega_g$. The ground and excited states are labeled by the indices g and e respectively. By introducing the Rabi frequency for a two-level atom

$$\Omega = \frac{E}{\hbar}\langle e|\mu|g\rangle, \tag{2.9}$$

these differential equations can be simplified to

$$\frac{\partial c_g(t)}{\partial t} = i\Omega^* c_e(t)e^{-i\omega_a t} \tag{2.10}$$

and

$$\frac{\partial c_e(t)}{\partial t} = i\Omega c_g(t)e^{i\omega_a t}, \tag{2.11}$$

where we have ignored the spatial dependance of the oscillating electric field.

Generally it is possible to solve these equations by transforming them into a rotating frame. Here we will follow another ansatz [8] and substitute the coefficients $c_g(t)$ and $c_e(t)$ with

$$c'_g(t) = c_g(t) \tag{2.12}$$

and

$$c'_e(t) = c_e(t)e^{-i\delta t}, \tag{2.13}$$

where $\delta = \omega_l - \omega_a$ defines the detuning from resonance. By making this substitution and making the Rotating Wave Approximation [9] one derives the following equations [10]

$$i\hbar\frac{dc'_g(t)}{dt} = c'_e(t)\frac{\hbar\Omega}{2} \tag{2.14}$$

and

$$i\hbar\frac{dc'_e(t)}{dt} = c'_g(t)\frac{\hbar\Omega}{2} - c'_e\hbar\delta. \tag{2.15}$$

It is now possible to diagonalize the matrix for the perturbative part of the Hamiltonian to the following form

$$H' = \frac{\hbar}{2}\begin{pmatrix} -2\delta & \Omega \\ \Omega & 0 \end{pmatrix}, \tag{2.16}$$

thus the shifted energy levels are given by

$$E_{g,e} = \frac{\hbar}{2}(-\delta \pm \Omega'), \tag{2.17}$$

where $\Omega' \equiv \sqrt{\Omega^2 + \delta^2}$. If we assume $\Omega \ll \delta$ the energy levels are shifted by

$$\Delta E_{g,e} = \pm\frac{\hbar\Omega^2}{4\delta} \tag{2.18}$$

respectively.

Similarly, if we assume $\Omega \gg |\delta|$ the levels shift by

$$\Delta E_{g,e} = \pm sgn(\delta)\frac{\hbar\Omega}{2}\,. \tag{2.19}$$

A schematic for the two-level energy shift is shown in fig. 2.1.

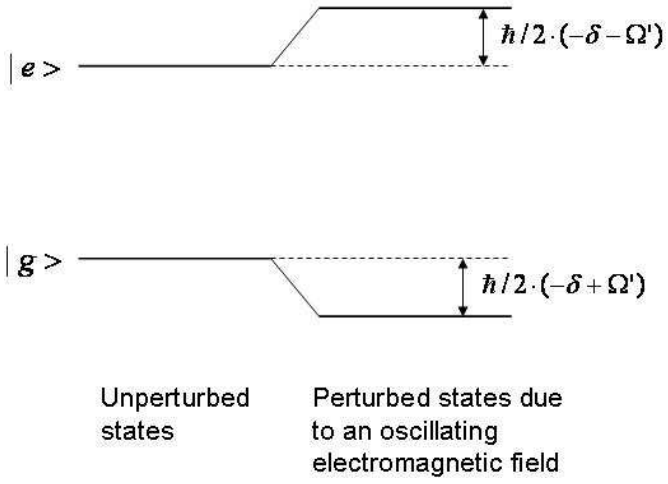

Figure 2.1: Schematic of the energy shift due to a periodic perturbation in a two-level atom.

The potential created by the energy shift can be used to trap atoms. The force due to the potential is a consequence of the dipole moment and is therefore called dipole force,

$$\vec{F}_{g,e} = -\nabla E = \mp \frac{\hbar}{4\delta} \nabla \Omega^2 \propto \frac{1}{\delta} \nabla I. \tag{2.20}$$

The dipole force is proportional to the intensity of the light and inversely proportional to the detuning of the light-frequency from the resonance frequency. Since the detuning from resonance can be either positive or negative, i.e. blue or red detuned, one should consider two separate cases. In case of blue detuned light, $\delta > 0$, the energy shift of the ground state is positve and the dipole force repulses atoms from the intensity maximum. Therefore atoms will not be trapped in the beam. On the other hand, it is doable to exert an attractive dipole force if $\delta < 0$. Thus it is possible to trap atoms in a red detuned laser beam, as it is done in an optical tweezer.

2.3 Interaction of a multi-level system with non-resonant light

Although there are many cases where the two-level approximation is justified, we will now consider the more general case of a multi-level atom by going back to the Schrödinger-equation (eq.2.1) and using time-dependant perturbation theory to solve the differential equation.

In the second order expansion we get the following expression for the coefficients $c_m(t)$,

$$c_m(t) - c_m(0) = -\frac{1}{\hbar^2}\int_0^t dt' \int_0^{t'} dt'' \sum_k \vec{\mu}_{nk}\vec{E}(\vec{r},t')\vec{\mu}_{km}\vec{E}(\vec{r},t'')e^{i\omega_{nk}t'}e^{i\omega_{km}t''}, \tag{2.21}$$

where the sum has to be evaluated over all possible states. For further analysis we insert the complex electric field $E(t) = \frac{1}{2}E_0 e^{i\omega_l t} + c.c.$, where we neglect the spatial dependance again. Thus we obtain

$$\begin{aligned} c_m(t) - c_m(0) &= -\frac{1}{4\hbar^2}\int_0^t dt' \int_0^{t'} dt'' \sum_k \vec{\mu}_{nk}E_0(t')\left(e^{i\omega_l t'} + e^{-i\omega_l t'}\right) \\ &\quad \times \vec{\mu}_{km}E_0(t'')\left(e^{i\omega_l t''} + e^{-i\omega_l t''}\right)e^{i\omega_{nk}t'}e^{i\omega_{km}t''}, \end{aligned} \tag{2.22}$$

where we have avoided the Rotating Wave Approximation.

Assuming the atom to be in state $|m\rangle$ we can rewrite the coefficients as complex phase $e^{i\phi(t)}$. The equation above then reads

$$\begin{aligned} 1\cdot e^{i\phi(t)} - const. &= -\frac{1}{4\hbar^2}\int_0^t dt' \int_0^{t'} dt'' \sum_k \vec{\mu}_{nk}E_0(t')\left(e^{i\omega_l t'} + e^{-i\omega_l t'}\right) \\ &\quad \times \vec{\mu}_{km}E_0(t'')\left(e^{i\omega_l t''} + e^{-i\omega_l t''}\right)e^{i\omega_{nk}t'}e^{i\omega_{km}t''}. \end{aligned} \tag{2.23}$$

By differentiating and averaging over one period this becomes

$$\langle\dot{\phi}\rangle = -\frac{|E_0|^2}{4\hbar^2}\sum_k |\vec{\mu}_{km}|^2\left(\frac{1}{\omega_{km}+\omega_l} - \frac{1}{\omega_{km}-\omega_l}\right). \tag{2.24}$$

The energy shift for the level m is then seen to be

$$\Delta E_m = \hbar\langle\dot{\phi}\rangle = -\frac{|E_0|^2}{\hbar}\sum_k |\vec{\mu}_{km}|^2\left(\frac{1}{\omega_{km}+\omega_l} - \frac{1}{\omega_{km}-\omega_l}\right) \tag{2.25}$$

and for the ground state

$$\Delta E_g = -\frac{|E_0|^2}{4\hbar}\sum_k |\vec{\mu}_{kg}|^2\left(\frac{1}{\omega_{kg}+\omega_l} - \frac{1}{\omega_{kg}-\omega_l}\right). \tag{2.26}$$

A comparison with the classical result $\Delta E_g = -\frac{\alpha(\omega)}{2}|E_0|^2$ gives the quantum-mechanical description for the polarizability $\alpha(\omega)$ [11]

$$\alpha(\omega) = -\frac{1}{2\hbar}\sum_k |\vec{\mu}_{kg}|^2\left(\frac{1}{\omega_{kg}+\omega_l} - \frac{1}{\omega_{kg}-\omega_l}\right). \tag{2.27}$$

In fig. 2.2 we show the AC-Stark shift for the Sodium ground state and the $3^2P_{3/2}(F=0)$ excited state as an example. The poles appear due to resonant transitions.

2.4 Dipole matrix elements, Einstein-coefficients and the AC-Stark shift

In order to calculate the AC-Stark shift it is necessary to evaluate the dipole matrix elements

$$\mu_{jk} = \langle j|\mu|k\rangle = \langle j|er_q|k\rangle. \tag{2.28}$$

Here e denotes the charge of an electron, r the electron coordinate and q the polarization of the incident electric field.

Since in alkali atoms hyperfine splittings play an important role, the eigenstates of the atoms have to be expressed in the F-basis. In the following section we will label the states $|k\rangle$ by the quantum numbers J_k and F_k for the angular momenta and the

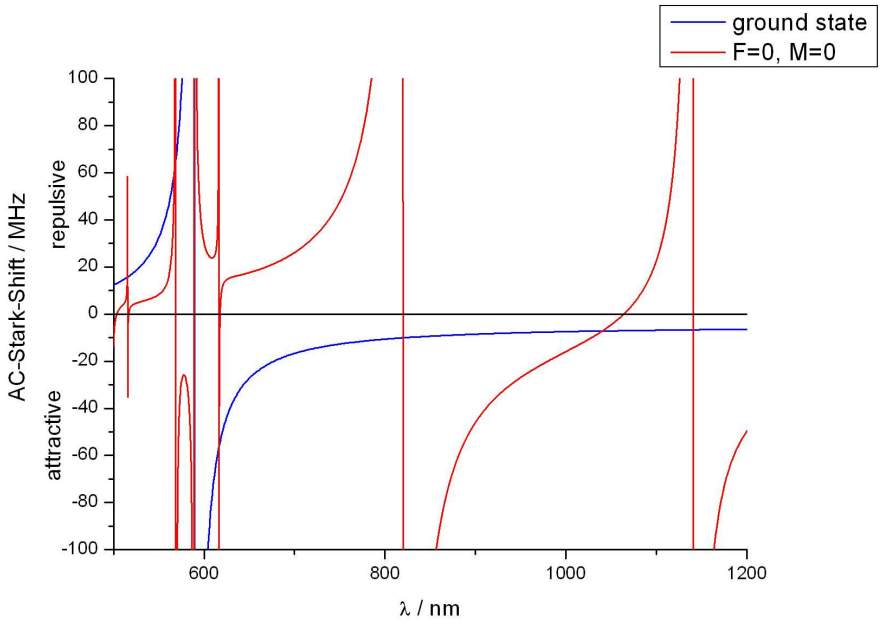

Figure 2.2: Plot of the AC-Stark shift. Numerical values are for a beam with P=1W, w_0=10μm and π-polarized light; the hyperfine structure belongs to the $3^2P_{3/2}$ state. The potential is attractive for $\Delta E < 0$ and repulsive for $\Delta E > 0$.

magnetic quantum number M_k. The dipole moment therefore reads

$$\mu_{jk} = e\langle J_k F_k M_k | r_q | J_j F_j M_j \rangle. \tag{2.29}$$

In general, the value of the dipole matrix element will depend on the polarization of the incoming beam; $q = \pm 1$ corresponds to circular ($\sigma^{\pm}$) polarised light, for linear (π) polarised light q equals 0.

The dipole matrix elements can be transformed into reduced matrix elements by applying the Wigner-Eckart Theorem [12]

$$\langle J_k F_k M_k | r_q | J_j F_j M_j \rangle = (-1)^{J_k - M_k} \begin{pmatrix} J_k & 1 & J_j \\ -M_k & q & M_j \end{pmatrix} \langle J_k F_k \| r \| J_j F_j \rangle. \tag{2.30}$$

On the right-hand side of eq. 2.30 we succeeded in separating the geometry and symmetry from the dynamics of the system using a reduced matrix element. The term

in brackets describes a Wigner-3j-symbol, which includes the selection rules for optical transitions. It is related to the Clebsch-Gordan-coefficients via the following equation

$$\begin{pmatrix} J_k & 1 & J_j \\ -M_k & q & M_j \end{pmatrix} = (-1)^{J_k-1-M_j} \sqrt{(2J_j+1)}\ \langle J_k\ -M_k, 1q|J_j\ -M_j\rangle. \tag{2.31}$$

Further evaluation of the reduced matrix element is necessary in order to calculate the dipole matrix element. The reduced matrix element in the F-basis can be transferred into the J-basis by factoring out the F-dependance,

$$\langle I_k J_k F_k \| r \| I_j J_j F_j\rangle = (-1)^{1+J_k+I_j+F_j} \sqrt{2F_j+1}\sqrt{2F_k+1} \begin{Bmatrix} J_k & I_j & F_k \\ F_j & 1 & J_j \end{Bmatrix} \langle J_k \| r \| J_j\rangle. \tag{2.32}$$

The term in curled brackets represents a Wigner-6j-symbol.

By inserting eq. 2.30 and 2.32 into 2.28 we express the matrix element as

$$\begin{aligned} \mu_{jk} &= e\langle J_k F_k M_k | r_q | J_j F_j M_j\rangle \\ &= e \cdot (-1)^{1+J_k+I+F_j+J_k-M_k} \begin{pmatrix} J_k & 1 & J_j \\ -M_k & q & M_j \end{pmatrix} \\ &\quad \times \sqrt{2F_j+1}\sqrt{2F_k+1} \begin{Bmatrix} J_k & I & F_k \\ F_j & 1 & J_j \end{Bmatrix} \langle J_k \| r \| J_j\rangle. \end{aligned} \tag{2.33}$$

We can connect the reduced matrix element $\langle J' \| r \| J\rangle$ with the Einstein-coefficients A_{jk} for spontaneous emission, respectively the inverse of the partial lifetime [10],

$$A_{kj} = \frac{1}{\tau_{kj}} = \frac{\omega_{kj}^3}{3\pi\epsilon_0\hbar c^3} \frac{1}{2J_k+1} |\langle J_k \| e\vec{r} \| J_j\rangle|^2. \tag{2.34}$$

Hence the dynamics of the system are included in the Einstein-coefficients, while the geometrical properties are represented by the Wigner-symbols. By applying eq. 2.34 and eq. 2.33 we get the following result for the energy shift [13],

$$
\begin{aligned}
\Delta E_j &= \sum_k \frac{|\mu_{kj}|^2 E^2}{\hbar}\left(\frac{1}{\omega_{kj}+\omega_l}-\frac{1}{\omega_{kj}-\omega_l}\right) \\
&= \sum_k \frac{E^2}{\hbar}\left(\frac{1}{\omega_{kj}+\omega_l}-\frac{1}{\omega_{kj}-\omega_l}\right) A_{kj}\frac{3\pi\epsilon_0\hbar c^3}{\omega_{kj}^3}(2J_k+1) \\
&\quad |e\cdot(-1)^{1+J_k+I+F_j+J_k-M_k}\sqrt{2F_j+1}\sqrt{2F_k+1}\begin{pmatrix} J_k & 1 & J_j \\ -M_k & q & M_j\end{pmatrix}\begin{Bmatrix} J_k & I & F_k \\ F_j & 1 & J_j\end{Bmatrix}|^2 \\
&= 3\pi c^2 I\sum_k \frac{A_{kj}(2J_k+1)}{\omega_{kj}^2\cdot(\omega_l^2-\omega_{kj}^2)} \\
&\quad \times|\sqrt{2F_j+1}\sqrt{2F_k+1}\begin{pmatrix} J_k & 1 & J_j \\ -M_k & q & M_j\end{pmatrix}\begin{Bmatrix} J_k & I & F_k \\ F_j & 1 & J_j\end{Bmatrix}|^2. \qquad (2.35)
\end{aligned}
$$

The sum of the Einstein coefficients and the corresponding transition strengths include the contributions from the possible dipole transitions in the atom. The relative transition strengths depend on the involved angular momenta J and F, the projection M and the polarization of the laser beam and are given by the geometry of the system which we have expressed by the Wigner-3j and Wigner-6j-symbols. Nevertheless, the absolute value of the AC-Stark shift is determined by the intensity of the laser beam.

Chapter 3

Magic Wavelength

The concept of a magic wavelength is mostly discussed in connection with time and frequency measurements. Today time and frequency standards are determined by Cesium fountain clocks as NIST-F1, where transitions are induced in a microwave-cavity [14]. Although frequency is already the most precisely measurable quantity, frequency measurements would be greatly improved by exploiting optical instead of microwave transitions.

For an optical clock, ultracold neutral atoms have to be trapped in order to minimize Doppler-Shifts. Optical traps have the disadvantage of shifting the energy levels, where the magnitude of the shift is proportional to the intensity of the beam used to create the trap, as we have shown in the previous chapter. In general, these shifts are different for different atomic levels, and the resonance frequency therefore depends on the trapping potential, i.e. the exact position of the atom inside the trap. Nevertheless, if the energy shifts are equal for the ground and the respective excited state the resonance frequency gets insensitive to the intensity of the laser beam and hence to the trapping potential. The wavelength with the above characteristics is called the magic wavelength [15].

An attractive trap at the magic wavelength provides the same potential for the ground and excited state. Hence the atoms held in this trap are not heated when a resonant transition is induced. The fluorescence signal contains information not only

on the transition frequency but also on the number of atoms trapped [16].

We have shown in chapter 2.2 that the energy shift for the ground and excited states are of equal magnitude but of opposite sign for a two-level atom. Hence it is impossible to find a magic wavelength in a two-level system. However, a magic wavelength is possible, but does not necessarily exist, in a multi-level system. Since all optical transitions depend on the polarization of the incident beam it is possible to find different magic wavelengths for different polarizations.

Magic wavelengths have already been calculated (and measured) in some atoms, Calcium [11] and Strontium [17] for example, but theoretical predictions of the magic wavelength are limited by the uncertainty in the Einstein-coefficients. Most Einstein-coefficients are only determined theoretically; the values depend strongly on the model and on the approximations used to calculate them.

3.1 Calculation of the magic wavelength in Sodium

In the previous chapter we derived an analytical expression for the AC-Stark shift (eq. 2.35). In order to minimize an error due to a limited number of transitions we took 32 different energy levels into account. Numerical values used to determine the magic wavelength in Sodium are taken from the NIST Databank [18]. Tab. 3.1 shows the numerical values for the magic wavelengths for π-polarized light for the different hyperfine levels.

state(s)	magic wavelength in nm
F=0; F=2; F=3, M=±2,0	1040 ± 8
F=1, M=0	1110 ± 3
F=1, M=±1	1020 ± 7
F=3, M=±1	1012 ± 9
F=3, M=±3	none

Table 3.1: Numerical values for the magic wavelengths of the ground state with the $3^2P_{3/2}$-state of Sodium for linear polarized light

The degeneracy of some of these levels, i.e. F=0 M=0 and the F=2 manifold are due to the same relative transition strengths. For trapping atoms with different magnetic sublevels it is desirable to have only one single magic wavelength for all of them. A universal magic wavelength like this does not exist in Sodium; nevertheless, for linear polarized light, a trapping wavelength around 1040nm looks promising since the potential is attractive for all states and does not change dramatically with the hyperfine level. Plots of the AC-Stark shift are shown in figs. 3.1 and 3.2. The poles are due to resonant transitions in Sodium atoms, e.g. at 589 nm.

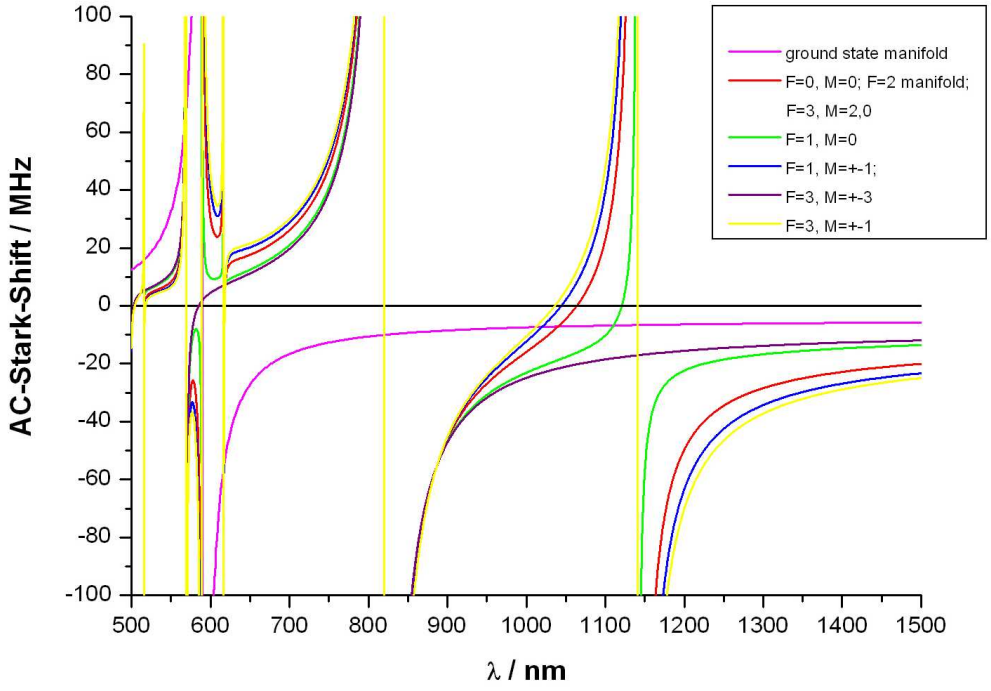

Figure 3.1: Plot of the AC-Stark shift. Numerical values are for a linearly polarized beam with P=1W, w_0=10μm and π-polarized light; the hyperfine structure belongs to the $3^2P_{3/2}$ state.

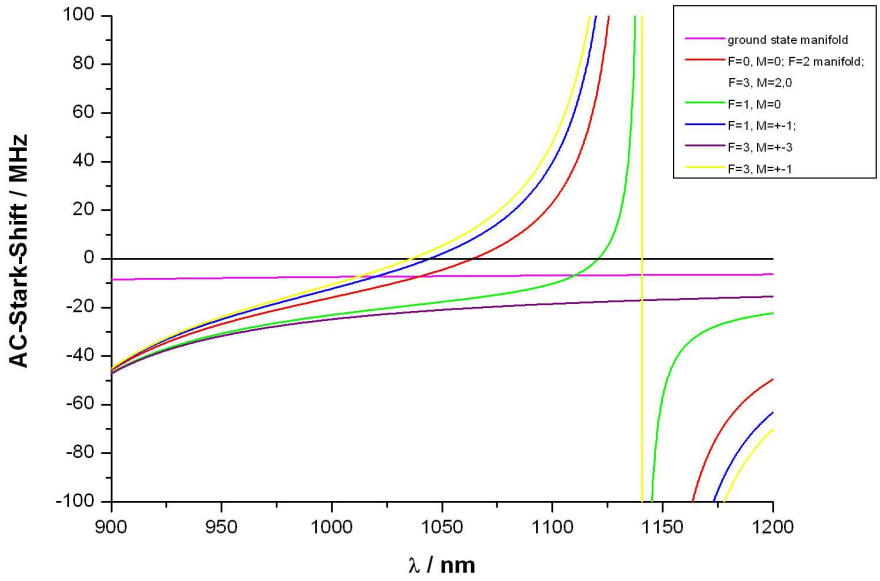

Figure 3.2: Plot of the AC-Stark shift in Sodium. Numerical values are for a linearly polarized beam with P=1W and w_0=10μm; detailed view around the magic wavelength; the hyperfine structure belongs to the $3^2P_{3/2}$ state.

Fig. 3.3 shows the AC-Stark shift for circularly (σ^+) polarized light.

A tweezer with circularly polarized light looks less promising compared to linearly polarized light. The degeneracy of most levels is removed, leading to even more individual magic wavelengths that are spreaded over a bigger wavelength range.

3.2 Magic wavelength in Rubidium

Using data from Safronova et al. (see also appendix C) we calculated the AC-Stark shift for Rubidium 87 [19]. Although individual magic wavelengths are found, there does not exist a wavelength which looks promising for trapping. The steep slope of the AC-Stark shift around the magic wavelengths near 1400nm leads to a very sensitive dependance on the trapping wavelength. The energy shift is also strongly dependant on the magnetic sublevel.

A plot of the AC-Stark shift is shown in fig. 3.4.

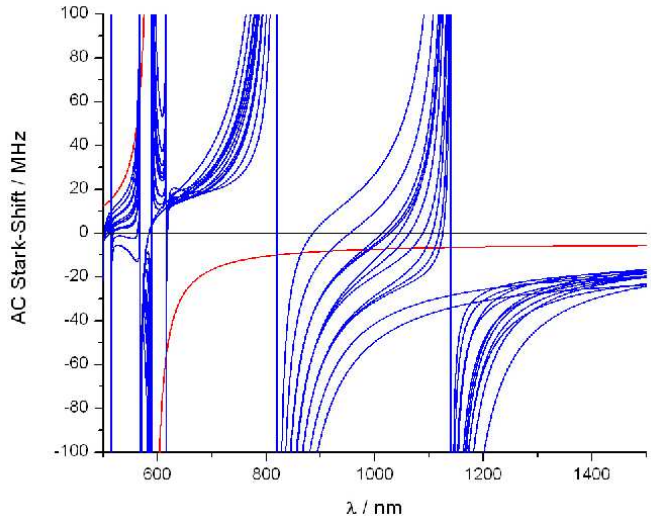

Figure 3.3: Plot of the AC-Stark shift in Sodium. Numerical values are for a circularly polarized beam with P=1W and w_0=10μm; the ground state manifold is shown in red, excited states ($3^2P_{3/2}$) are blue.

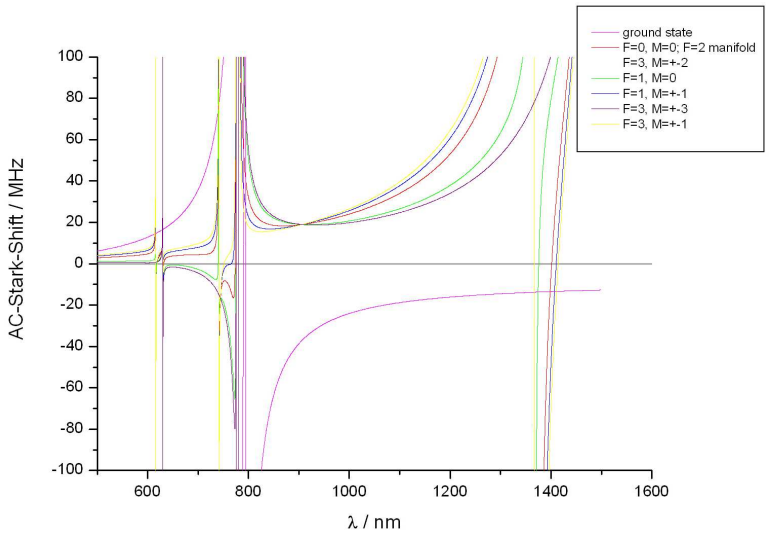

Figure 3.4: AC-Stark shift in Rubidium. Numerical values are for a linearly polarized beam with P=1W and w_0=10μm; the hyperfine structure belongs to the $5^2P_{3/2}$ state.

Chapter 4

Experiments on the magic wavelength

In this chapter we outline our efforts to determine the magic wavelength of Sodium. Although the measurements did not attain any meaningful results, we want to give a brief introduction to the idea of the measurement and shortly describe the experimental procedure.

4.1 Scattering Rate

In section 2.2 we described the interaction of a two-level atom with a monochromatic light field. However, an approach using coherent evolution of the amplitudes cannot describe spontaneous emission. In the two-level approximation this can be included using a density matrix formalism. The interaction of a two-level atom with electromagnetic radiation in the case of purely radiative damping can then be described by the optical Bloch equations [8]

$$\frac{d}{dt}\rho_{gg} = \frac{i\Omega}{2}(\tilde{\rho}_{ge} - \tilde{\rho}_{eg}) + \Gamma\rho_{ee} \tag{4.1}$$

$$\frac{d}{dt}\rho_{ee} = -\frac{i\Omega}{2}(\tilde{\rho}_{ge} - \tilde{\rho}_{eg}) - \Gamma\rho_{ee} \tag{4.2}$$

$$\frac{d}{dt}\rho_{ge} = -\frac{i\Omega}{2}(\rho_{ee} - \rho_{gg}) - (\frac{\Gamma}{2} + i\Delta)\tilde{\rho}_{ge}, \tag{4.3}$$

where ρ_{ij} are the matrix elements of the density operator, $\Omega = \frac{\vec{\mu}\cdot\vec{E}}{\hbar}$ is the resonant Rabi frequency, $\vec{\mu}$ the dipole operator, $\vec{E}$ the electric field, Γ the natural decay rate of the excited state e and $\tilde{\rho}_{ge} \equiv \rho_{ge}exp(-i\Delta t)$, $\tilde{\rho}_{ge} = \tilde{\rho}^*_{eg}$. The total steady-state photon scattering rate is then given by $\Gamma\rho_{ee}$ [20]

$$R_{sc} = \frac{\Gamma}{2}\frac{I/I_{sat}}{1 + (2\frac{\Delta}{\Gamma})^2 + \frac{I}{I_{sat}}}, \tag{4.4}$$

where $\frac{I}{I_{sat}} = 2\left(\frac{\Omega}{\Gamma}\right)^2$. This approximation is valid if the detuning Δ from the optical resonance is large, $\Delta \gg \Gamma$.

An additional light field causing an AC-Stark shift, corresponding to a detuning from resonance, should therefore decrease the scattering rate and consequently the amount of scattered light. Fig. 4.1 shows the scattering rate as a function of the detuning Δ for several values of $\frac{I}{I_{sat}}$. The natural decay rate Γ is taken to be $2\pi\cdot 9.795$MHz, corresponding to the Sodium D_2-line, which we use to trap and cool the atoms.

4.2 Experimental Setup

4.2.1 Oven and Zeeman-slower

Because of the low vapor pressure of Sodium ($P_v = 2.2 \cdot 10^{-11}$ torr [20]) it is necessary to heat the Sodium in an oven to about 500K. Our oven is not recirculating and therefore it has to be refilled after a few hundred hours of operation [21].

In order to be able to trap the atoms in a magneto-optical trap (MOT) (see section 4.2.2) the atoms in the effusive beam have to be decelerated to a few meters per second.

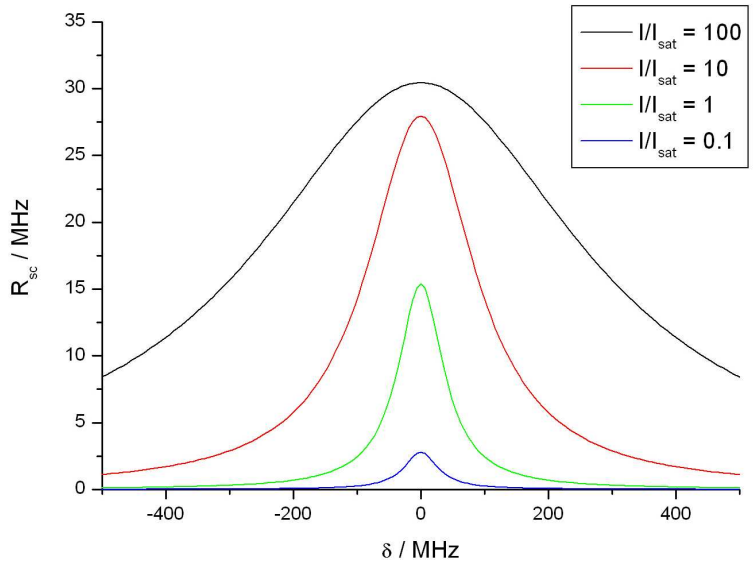

Figure 4.1: Scattering Rate dependance on the detuning δ for several values of $\frac{I}{I_{sat}}$. The natural decay rate Γ is $2\pi \cdot 9.795$MHz for the D_2-line in Sodium.

This can be achieved by scattering a sufficient number of photons from a counter-propagating beam. Atoms with different velocities have different Doppler-shifts, so the optical transition will be out of resonance after a certain number of scattering events. A resonant transition can be maintained by changing the magnetic hyperfine splittings using an external magnetic field, tuned to compensate for the decreasing Doppler-shift of the decelerating atoms. In a low magnetic field the magnetic energy levels split proportionally to the magnitude of the field. This is called the anomalous Zeeman-effect and is used in a Zeeman-slower to maintain a resonant transition between the ground and the respective excited state. The slowing transition in our setup is the $|F = 2, M = 2\rangle \rightarrow |F = 3, M = 3\rangle$ transition and is excited by a dye laser (Coherent 899-21).

4.2.2 Magneto-Optical Trap

After leaving the Zeeman-slower the atoms that are sufficiently slowed are trapped in a magneto-optical trap (MOT). Two coils in an Anti-Helmholtz-configuration provide

a quadrupole field with a magnetic field gradient in radial (ρ-) and axial (z-) direction, where

$$\frac{dB_z}{dz} = 2\frac{dB_\rho}{d\rho}. \tag{4.5}$$

In addition to the magnetic field gradient there are three pairs of counter-propagating beams, red-detuned from the resonance at zero magnetic field; a schematic of the alignment is shown in fig. 4.2. If a trapped atom moves out of the zero magnetic field at the center of the trap, the magnetic sublevels will split according to the magnitude

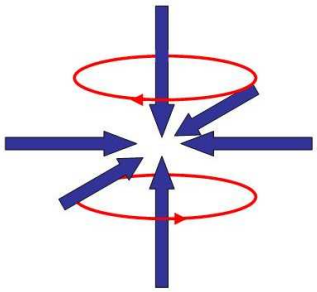

Figure 4.2: Schematic of the beam configuration in a magneto optical trap (MOT), the current in the Anti-Helmholtz-coils (red) flows opposite, the MOT beams are represented by the blue arrows

of the magnetic field. Therefore the detuning decreases with an increasing distance from the center of the magnetic field. If the polarizations of the two opposing beams are aligned correctly, there will be more light scattered from one than from the other and the atom driven back towards the center of the trap, i.e. an atom moving to the right scatters more σ^--polarized light. In fig. 4.3 we have shown a schematic for the magnetic detuning in a 1-D-MOT, which can easily be extended to three dimensions.

The beams in our setup are 20MHz red detuned from the $3^2S_{1/2}(F = 2) \rightarrow 3^2P_{3/2}(F' = 3)$ transition; the magnetic field gradient in the axial direction is 15G/cm.

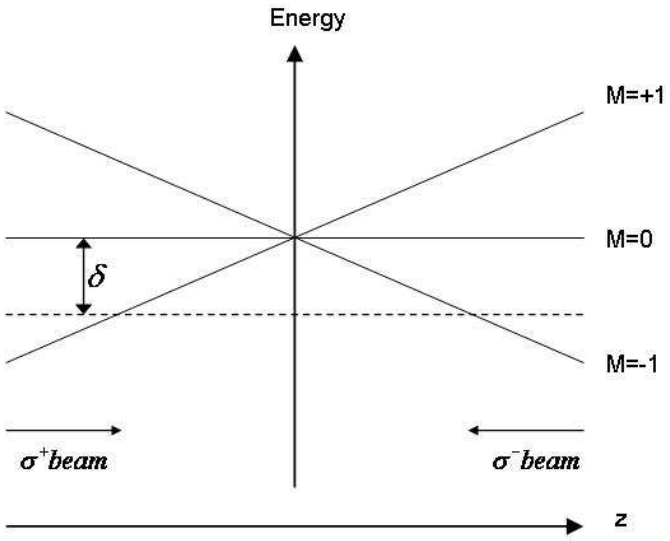

Figure 4.3: Sketch of the Zeeman-Shift in a 1-D MOT. The dashed line represents the red detuned MOT-beam frequency. The position dependant Zeeman-shift changes the detuning from the resonance frequency [8].

4.3 Experimental procedure

After loading about 10^9 atoms into the MOT we collected the scattered light and focused it down onto an avalanche photo diode (APD). By introducing an AC-Stark shift with a YAG-laser (IPG Photonics YLD-10) at 1064nm the fluorescence signal of the MOT should change slightly. Since the desired signal is small compared to the background fluorescence we intended to use a lock-in amplifier (SRS 510) to extract the signal. We therefore pulsed the YAG-laser with frequencies between 1kHz and 10kHz.

The first signal we got was due to light directly scattered from the YAG beam into the APD. We therefore put additional shielding around the APD and could remove scattered light at a wavelength of 1064nm.

We created a MOT with a diameter of approximately $500\mu m$ and variied the beam waist of the YAG-laser between $190\mu m$ and $400\mu m$. The predicted AC-Stark shift δ due to a 6W YAG-beam with a waist of $400\mu m$ is 49.4kHz in about 49% of the atoms, assuming the MOT to be spherical and of equal density. Using eq. 4.4 we can calculate

the scattering rate in the MOT with the detuning $\Delta = 20MHz$ of the MOT-beams and the scattering rate in presence of the YAG-light with the total detuning $\Delta_{tot} = \Delta + \delta$. Thus the expected change in the fluorescence signal is about 2% relative to the flourescence without the YAG-beam. Nevertheless, we were not able to detect a change in the fluorescence signal.

The attempt to introduce a frequency modulation of the MOT-light itself using two DDS (Direct Digital Synthesis) failed. The switching of the DDS resulted in transients that were picked up by the MOT fluorescence. Changing the frequency using a frequency generator (HP 0.1-2010 GHz FG) with external modulation we succeeded to induce a change in flourescence. At a modulation frequency of 10kHz we could detect down to a 2kHz change in the MOT-frequency. The corresponding change in the flourescence signal was 0.48%.

A stronger effect of the AC-Stark shift is expected at a wavelength of 532nm, far away from a magic wavelength. Hence we followed the same experimental procedure using a Verdi laser (Coherent Verdi V10) instead of the YAG-laser; but we still could not detect a meaningful signal. It is possible that the changing magnetic field in the MOT complicates the measurements in a way we were not considering.

In our future experiments we will not drive a clock transition, therefore we are not obliged to use a magic wavelength. Moreover, since the atoms are in different hyperfine states, a trap cannot be at a magic wavelength for all the atoms. Nevertheless, it is advantageous to be near a magic wavelength to avoid a strong heating of the atoms.

Chapter 5

Stimulated Raman transitions

A Raman transition is a two-photon process that couples two different energy levels and transfers population from one state into the other. This is done by absorbing one photon from a monochromatic light source (usually a laser) and reemitting a photon with a different frequency. *Stimulated* Raman transition means that the emission is also driven by an external monochromatic field (second laser beam). For an efficient population transfer, the beams should be detuned by the frequency corresponding to the energy difference of the two coupled states.

In section 5.1 we will give a brief overview of stimulated Raman transitions, before we present the fundamental limits in section 5.2. The following sections will present a theoretical description of stimulated Raman processes, first for a simple three-level system in section 5.3, then generalizing to multi-level systems in section 5.4. Lastly, we will describe the effects due to an external magnetic field.

5.1 General description of spatially resolved stimulated Raman transitions

The ground state $^2S_{1/2}$ in Sodium splits into two hyperfine levels with F=1 and F=2. The difference frequency between those two states is 1.772GHz. The laser we use to cool and trap the atoms in a MOT, is tuned to the $|3^2S_{1/2}, F = 2\rangle \rightarrow |3^2P_{3/2}, F = 3\rangle$

transition. Therefore only atoms in the $|F = 2\rangle$ ground state will be excited by our laser and start fluorescing until they finally decay into the $|F = 1\rangle$ state. Ususally, a repump laser, tuned to the $|3^2S_{1/2}, F = 1\rangle \rightarrow |3^2P_{3/2}, F = 2\rangle$ transition, is used to transfer atoms out of the dark state back to the $|F = 2\rangle$ ground state.

Let us assume now all atoms start in the $|F = 1\rangle$ ground state. In a direct transition using a radio frequency pulse spatial resolution can be achieved by shifting the energy levels of the two hyperfine ground states by applying a magnetic field gradient. This leads to a spatially varying resonance frequency ω_0. By tuning the frequency of the radio field one can select a small region around x_0 in which the atoms will make a transition, if a pulse with the appropriate intensity and duration is applied. A simplified scheme of the one-photon transition is shown in fig. 5.1, where we have assumed that only the final state $|f\rangle$ is dependant on the magnetic field. The resolution is given by the width of the atomic distribution that is excited around a particular x_0.

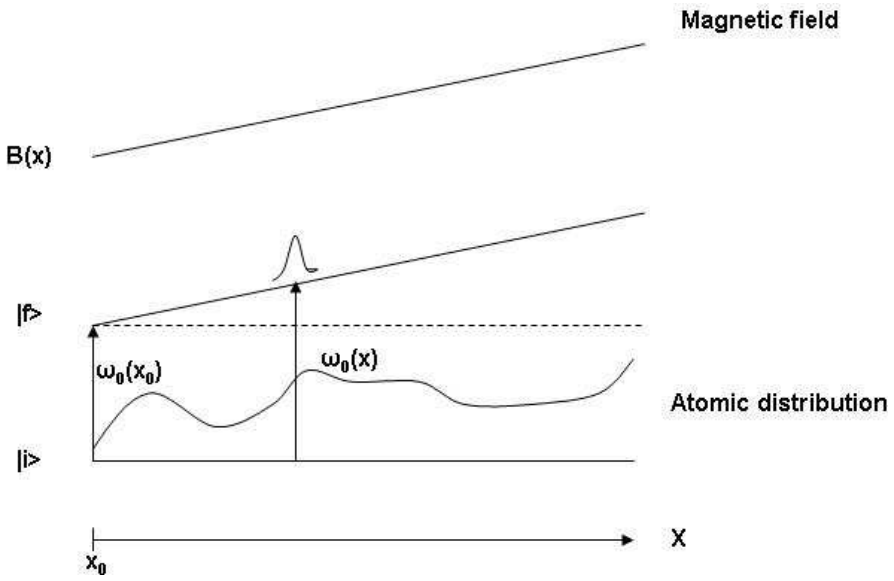

Figure 5.1: Simplified scheme of a resonant transition with spatial resolution; the resonance frequency ω_0 is space-dependant, i.e. the resonance frequency ω_0 at x_0 is not in resonance at point x. For simplicity we have assumed that only the final state $|f\rangle$ is dependant on the magnetic field.

The scheme for a Resonant Raman transition looks fairly similar, as can be seen in fig. 5.2. Instead of a resonant one-photon transition a resonant two-photon transition occurs. Two frequencies ω_1 and ω_2 are combined into one excitation pulse, where the difference frequency $\omega = \omega_1 - \omega_2$ equals the differency frequency between the initial and the final state. Both frequencies, ω_1 and ω_2 are off-resonant; the detuning to the intermediate level $|I\rangle$ is given by Δ.

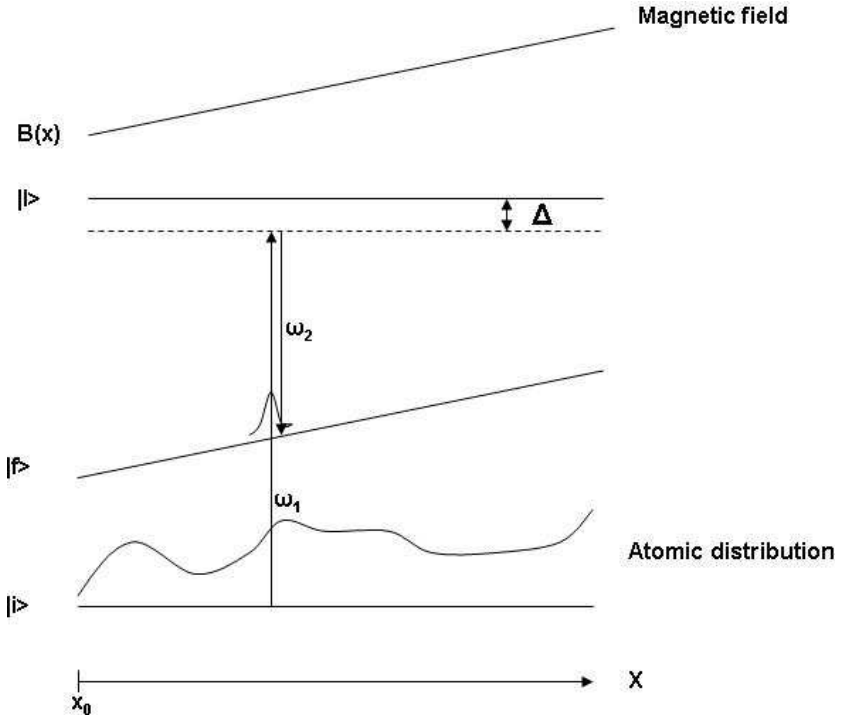

Figure 5.2: Simplified scheme of a resonant Raman transition with spatial resolution;the resonance frequency is space-dependant. For simplicity we have assumed that only the final state $|f\rangle$ is dependant on the magnetic field. The two frequencies ω_1 and ω_2 are off-resonance with an intermediate level $|I\rangle$. The detuning is given by Δ.

5.2 Limitations for spatially resolved Raman transitions

In the following section we want to present the fundamental limits for spatially resolved Raman transitions [22]. In addition to considering the spectral resolution, we must also

take into account the velocity of the atoms and their accelerations due to the differential force exerted by the potential for the initial and final state.

5.2.1 Spectral resolution limit

During the Raman process one photon is absorbed and another photon of almost the same frequency is emitted into a co-propagating field. Thus the net momentum change of the atom is negligible. The use of a co-propagating configuration avoids a velocity-selection due to Doppler-Shifts which has been observed by Kasevich et al. using a counter-propagating beam configuration [23]. Raman-induced resonance imaging using co-propagating laser fields has been used by Thomas et al. for precision position measurements of moving atoms [24], [25].

If the detuning of both Raman pulses from resonance is large enough to avoid a population of an excited state, incoherent transitions between the two ground states can be avoided. Therefore, the life-time of the ground states determines the bandwidth of the Raman transition. Since the lifetime of the ground states is long, we are able to neglect the bandwidth of the Raman transition.

The difference in the Raman beams can be created by passing one beam through an acousto-optic modulator (AOM). By equalizing the optical path length it is possible to minimize the frequency jitter in the difference frequency; in this limit the stability of the difference frequency is then given by the AOM and is usually small and negligible.

In the limit of a very stable difference frequency the Fourier-Theorem gives the frequency resolution of the Raman process,

$$\Delta\omega \approx \frac{1}{T}. \tag{5.1}$$

For simplicity we assume the initial state $|i\rangle$ to be independant of the magnetic field. If the frequency shift of the final state $|f\rangle$ varies linearly with the position, the force F exerted by the magnetic field on the final state is uniform and the frequency shifts as $\Delta\omega = \frac{\Delta E}{\hbar} = \frac{F}{\hbar}\Delta x$. The quantity $\frac{F}{\hbar}$ is the spatial tuning rate, which determines the spatial

variation of the resonance transition frequency. Combining this with eq. 5.1, we yield the spectral resolution limit

$$\Delta x_{sp} = \frac{\hbar}{FT} \ . \tag{5.2}$$

5.2.2 Velocity-limited resolution

The spatial resolution is not only influenced by the spectral resolution but also by atomic motion. Atoms with a certain velocity v_x along the measurement axis will leave the resonant region after having made the transition from the initial state $|i\rangle$ to the final state $|f\rangle$. Hence the velocity-limited resolution is

$$\Delta x_{vel} = v_x T. \tag{5.3}$$

The velocity-limited resolution increases with a decreasing pulse duration, and so a short pulse duration is desirable. However, the spectral resolution limit will decrease with a decreasing pulse time. The optimal pulse duration can be found using eq. 5.2 and 5.3. The velocity-limited resolution is given by

$$\Delta x_{vel} = \sqrt{\frac{\hbar v_x}{F}}. \tag{5.4}$$

5.2.3 Acceleration-limited resolution and the Heisenberg uncertainty principle

Atoms do not only move because of their initial velocity; they will also be accelerated by the force due to the energy gradient. This should not be confused with the fact that the net momentum due to absorption and emission of photons is negligible. The acceleration-limitied resolution is

$$\Delta x_{acc} = \frac{F}{2m} T^2, \tag{5.5}$$

where m is the atomic mass. By setting $\Delta x_{sp} = \Delta x_{acc}$ one finds the optimal pulse duration

$$T_{acc} = \left(\frac{2\hbar m}{F^2}\right)^{1/3} \tag{5.6}$$

and the acceleration limited resolution thus becomes

$$\Delta x_{acc} = \left(\frac{\hbar^2}{2mF}\right)^{1/3}. \tag{5.7}$$

Let us assume that only the final state is shifted by the potential. The transition between the initial state $|i\rangle$ and the final state $|f\rangle$ can occur at any time during the pulse time T, and so the uncertainty in the final momentum of the atoms is $\Delta p = FT$. Simple multiplication with the spectral resolution limit (eq. 5.2) leads to the fundamental limit given by the uncertainty relation between space and momentum

$$\Delta x \Delta p = \hbar. \tag{5.8}$$

μm

5.3 Raman transitions in a three level atom

The total electro-magnetic field driving a stimulated Raman transition can be described by the sum of the two individual light beams with frequencies ω_1 and ω_2,

$$\vec{E}(\vec{r},t) = \frac{1}{2}\cdot\left(\vec{E}_1\cdot e^{i(\vec{k}\cdot\vec{r}-\omega_1 t)} + \vec{E}_1\cdot e^{-i(\vec{k}\cdot\vec{r}-\omega_1 t)} + \vec{E}_2\cdot e^{i(\vec{k}\cdot\vec{r}-\omega_2 t)} + \vec{E}_2\cdot e^{-i(\vec{k}\cdot\vec{r}-\omega_2 t)}\right). \tag{5.9}$$

There exist three possible configurations of a three-level system with the initial state $|i\rangle$, an intermediate state $|I\rangle$ and a final state $|f\rangle$, that is driven by a two-photon process, usually called the ”ladder”, ”V” or ”lambda” configurations, which are schematically shown in fig. 5.3 [26]. A stimulated Raman transition between two hyperfine levels of the ground state corresponds to the Λ-configuration.

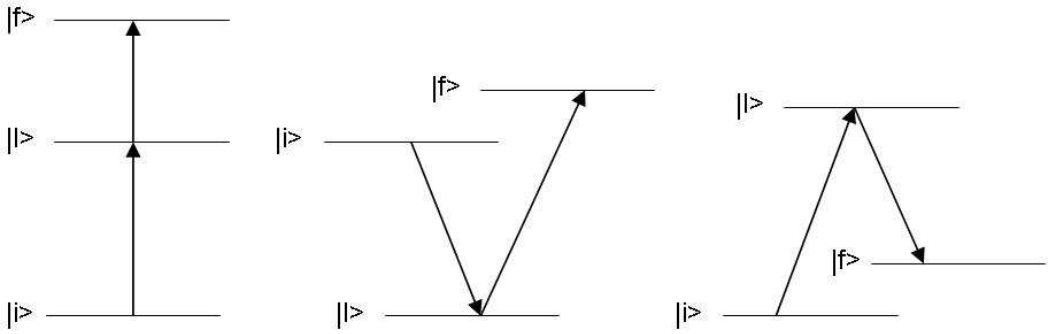

Figure 5.3: Possible configurations of a three-level system driven by a two-photon process, from left to right: ladder-configuration, V-configuration, Λ-configuration

5.3.1 Three-level amplitude equations

In chapter 2 we developed the coherent amplitude formalism for the interaction of an atom with an electric field. The amplitude equations in a three level system and with two monochromatic light sources become [27]

$$\dot{c}_i = \frac{i\Omega_1^*}{2} c_I e^{i\Delta_1 t}, \tag{5.10}$$

$$\dot{c}_f = \frac{i\Omega_2^*}{2} c_I e^{i\Delta_2 t} \tag{5.11}$$

and

$$\dot{c}_I = \frac{i\Omega_1}{2} c_i e^{-i\Delta_1 t} + \frac{i\Omega_2}{2} c_f e^{-i\Delta_2 t}, \tag{5.12}$$

where the Rabi frequencies Ω_1 and Ω_2 are defined by

$$\Omega_1 = \frac{-E_1}{\hbar} \langle I|\mu|i\rangle \tag{5.13}$$

and

$$\Omega_2 = \frac{-E_2}{\hbar} \langle I|\mu|f\rangle; \tag{5.14}$$

Δ_1 and Δ_2 describe the detunings from the transition frequency,

$$\Delta_1 = \omega_1 - \omega_{Ii} \tag{5.15}$$

and

$$\Delta_2 = \omega_2 - \omega_{If}. \tag{5.16}$$

Here we have neglected the decay rate Γ of the intermediate level which is justified because of a negligible population due to large detunings. Furthermore the decay rate is negligible compared to the Rabi frequencies, $\Omega_1, \Omega_2 \gg \Gamma$. A sketch of the frequencies and detuning involved in a stimulated Raman process in a three-level atom is shown in fig. 5.4.

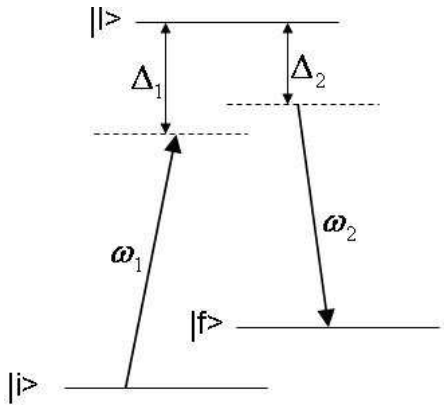

Figure 5.4: Schematic of the frequencies and detunings in a stimulated Raman process in a three-level atom.

5.3.2 Adiabatic Reduction to a two-level system

Eq. 5.12 can be integrated directly by neglegting the time-dependance of the coefficients c_i and c_f [28]. We can use the solution

$$c_I = -\frac{\Omega_1}{2\Delta_1} c_i e^{-i\Delta_1 t} - \frac{\Omega_2}{2\Delta_2} c_f e^{-i\Delta_2 t} \tag{5.17}$$

to adiabatically reduce the three-level amplitude equations to an effective two-level system,

$$\dot{c}_i = -i\nu_1 c_i - \frac{\beta}{2} c_f e^{i\delta t} \tag{5.18}$$

$$\dot{c}_f = -i\nu_2 c_f - \frac{\beta^*}{2} c_i e^{-i\delta t}, \tag{5.19}$$

where $\Delta_1 \approx \Delta_2 \equiv \Delta$ and $\delta = \Delta_1 - \Delta_2$. The AC-Stark shifts ν_m and the effective Raman-Rabi frequency β are then defined by

$$\nu_m \equiv \frac{|\Omega_m|^2}{4\Delta} \tag{5.20}$$

$$\beta \equiv -\frac{\Omega_1^* \Omega_2}{2\Delta}. \tag{5.21}$$

Eqs. 5.18 and 5.19 can be solved by substituting

$$c_i = a_i e^{-i\nu_1 t} \tag{5.22}$$

$$c_f = a_f e^{-i\nu_2 t}. \tag{5.23}$$

Doing this we can rewrite the set of differential equations as

$$\dot{a}_i = \frac{i\beta}{2} a_f \, e^{i(\delta - (\nu_2 - \nu_1))t} \tag{5.24}$$

and

$$\dot{a}_f = \frac{i\beta^*}{2} a_i \, e^{-i(\delta - (\nu_2 - \nu_1))t}. \tag{5.25}$$

If both light shifts are equal, $\nu_2 = \nu_1$, and the detuning δ from the resonant Raman transition vanishes, the solution of these equations is trivial. The final state probability then is

$$P_f(t \to \infty) = |c_f(t \to \infty)|^2 = |a_f(t \to \infty)|^2 = sin^2\left(\frac{|\beta|}{2}\tau\right), \tag{5.26}$$

where we have assumed the initial population of state $|f\rangle$ to be zero and a Raman pulse duration of length τ. $|\beta|\tau$ is commonly known as pulse area. A $\frac{\pi}{2}$-pulse will transfer

half the population while a π-pulse transfers the whole population from the initial into the final state.

We have assumed the light shifts ν_1 and ν_2 to be equal. Experimentally this can be achieved by tuning the intensities of the incident Raman beams. This becomes especially easy when driving a resonant transition between the two hyperfine ground states in Sodium (F=1 and F=2), since both states are shifted equally (see chapter 3). Thus if both beams have the same power and beam waist, i.e. the incident intensities are identical, AC-Stark shifts will be equalized.

In addition to the final state probability for the resonant case we must now consider the non-resonant case. We can solve the amplitude equation for the non-resonant case using perturbation theory and assuming $a_i(0) \approx 1$. We are then able to integrate eq. 5.25, where we again assume the light shifts ν_1 and ν_2 to be equal. For a square Raman pulse of length τ the final state amplitude a_f becomes

$$a_f(t \to \infty) = \int_{-\tau/2}^{\tau/2} \frac{i\beta^*}{2} e^{-i\delta t'} dt' = -\frac{\beta^*}{\delta} sin\frac{\delta\tau}{2}. \tag{5.27}$$

We may center the pulse around $t = 0$ without loss of generality. The general solution for the final state probability $|a_f(t \to \infty)|^2$ is then

$$P_f(t \to \infty, \delta) = \frac{\tau^2|\beta|^2}{4} sinc^2\left(\frac{\delta\tau}{2}\right), \tag{5.28}$$

where

$$sinc\ x \equiv \frac{sin\ x}{x}. \tag{5.29}$$

We find the exact solution for $\delta = 0$ to be nearly equal to the approximated solution given above. Hence we can identify eq. 5.28 as the product of eq. 5.26 with a $sinc^2$ line shape for small pulse areas. Nevertheless for pulse areas as large as 4π the line shape stays approximately constant [29] and we will therefore use

$$P_f(t \to \infty, \delta) = sin^2\frac{|\beta|\tau}{2} sinc^2\left(\frac{\delta\tau}{2}\right). \tag{5.30}$$

as the final state probability.

5.4 Raman transition in a multi-level atom

In general the selection rule $\Delta m_F = 0, \pm 1, \pm 2$ applies for a Raman transition. Nevertheless in alkali-atoms transitions from one hyperfine ground state into the other with $\Delta m = \pm 2$ are forbidden. This is easily understood by looking at the two-photon process in tensor notation and recalling that all alkali-atoms occupy a ground state with $J = 1/2$.

By combining two one-photon processes we can generally create three different tensor operators. The scalar operator $E_1 E_2^*$ vanishes for perpendicular polarized light beams. The vector operator $E_1 \times E_2^*$ causes Raman transitions with $\Delta m = 0, \pm 1$, see fig. 5.5. An outer product operator $E_1 \otimes E_2^*$ of rank 2 cannot be formed for atoms in a $J = 1/2$ ground state [30]. Therefore transitions with $\Delta m = \pm 2$ do not occur. By explicitly calculating the multiple paths between the initial and the final state the same result arises due to destructive interference.

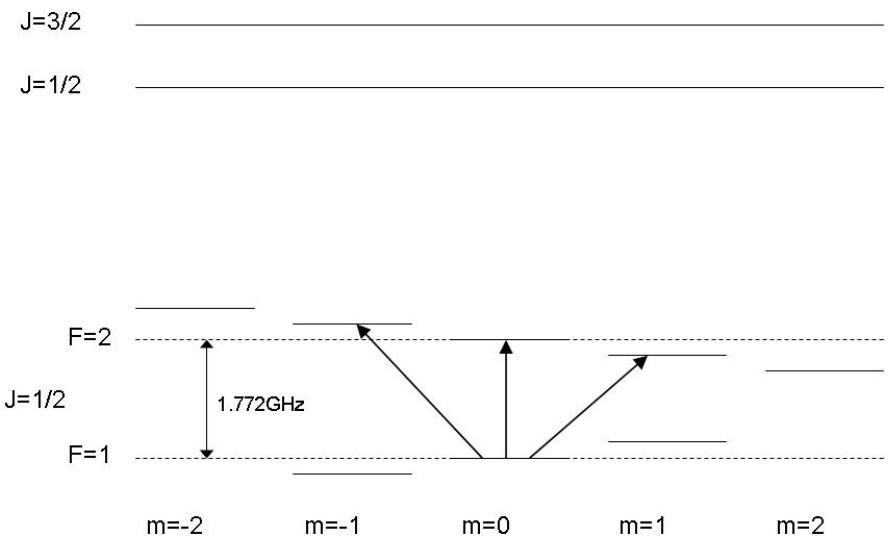

Figure 5.5: Possible Raman transitions between two hyperfine states with $J = 1/2$. For simplicity we assume all atoms to start in the $|F = 1, m = 0\rangle$ state. The detuning of 1.772GHz belongs to the Sodium ground state $^2S_{1/2}$. The splitting of the magnetic sublevels is according to the anomalous Zeeman-effect.

5.4.1 Multiple initial and final states

Each hyperfine level splits into (2F+1) magnetic sublevels. We therefore have to deal with three inital levels (F=1) and five final levels (F=2). In an external magnetic field the levels are split as shown in fig. 5.5, providing the possibility for a spatially resolved measurement. If this splitting is larger than the Raman transition linewidth, only one transition will be resonant. It is then possible to treat each transition as a separate two-level Raman process. The shift due to an external magnetic field is described in more detail in appendix B.2.

In the result for the final state probability we have to take into account the fact that the atoms are in different magnetic sublevels, where we can assume an equal distribution in each of these if there is no condition favorable for one above another. In addition to the detuning δ due to the difference frequency of the two laser beams another detuning $\delta_i^B(\vec{r})$ arises due to the magnetic field splitting of the magnetic hyperfine states. This detuning is therefore dependant on the magnetic state of an atom. Including the detuning due to the magnetic field splitting the final state probability develops to

$$P_f(t \to \infty, \delta) = \frac{1}{3} \sum_i sin^2 \frac{|\beta_i(\vec{r})|\tau}{2} sinc^2 \frac{(\delta - \delta_i^B(\vec{r}))\tau}{2}, \tag{5.31}$$

where we have to sum over all initial states.

5.4.2 Multiple intermediate states

In addition to multiple initial and final states we also have to take multiple intermediate levels into account. We have argued that we can treat multiple initial and final states separately. However, things are not quite as easy if one considers different intermediate levels. A treatment similar to the one in section 5.3 can be done by including additional intermediate levels. Adiabatic elimination of these levels results in an effective Raman-

Rabi frequency β given by

$$\beta_{fi} = -\sum_I \frac{\langle f|\mu E_2|I\rangle\langle I|\mu E_1|i\rangle}{2\hbar^2\Delta_I}, \tag{5.32}$$

which corresponds to a summation of all possible paths between the initial and the final state.

5.5 Raman transitions in a magnetic field

Before we explain the effect of a magnetic field on the effective Raman-Rabi frequency we will discuss the shift of the Raman resonance frequency $\delta_i^B(\vec{r})$. For simplicity we will now only examine the atoms starting in the $|F = 1, m_F = 0\rangle$ ground state, the two other states can be treated similarly. The possible Raman transitions from the initial level $|F = 1, m_F = 0\rangle$ (shown in fig. 5.5) correspond to a change in the magnetic sublevel of $\Delta m = 0, \pm 1$.

In presence of a magnetic field both initial and final state are shifted by

$$\Delta\omega(\vec{r}) = \frac{1}{\hbar}\, g\, m\, \mu_B\, B(\vec{r}), \tag{5.33}$$

where m is the quantum number of the final state, μ_B the Bohr-magneton and $B(\vec{r})$ the magnitude of the magnetic field at position $\vec{r}$. For the detuning from the Raman resonance frequency the absolute value of the single detunings is irrelevant. Rather, the difference of these is important,

$$\delta^B_{m_f,m_i}(\vec{r}) = \frac{1}{\hbar}(g_f\, m_f - g_i\, m_i)\mu_B B(\vec{r}) = \frac{1}{\hbar}\gamma_{m_f,m_i}\mu_B B(\vec{r}). \tag{5.34}$$

The effect of a magnetic field on the effective Raman-Rabi frequencies is more delicate. In the lab frame we define the polarizations of our two beams as $\{\hat{x}, \hat{y}\}$ and assume a propagation along the $\hat{z}$-axis. The cross product $\hat{x} \times \hat{y} = \hat{z}$ forms the rank one operator $T(1, 0)$, leading to transitions with $\Delta m = 0$. The atoms, however, may regard

the polarizations as any perpendicular combination of fields, i.e. $\{\hat{y}, \hat{z}\}$, which therefore allows transitions with $\Delta m = \pm 1$. The number of atoms making the transition from the initial to the final state remains independant of the local orientation of the atoms, because lab frame and atom frame are equivalent in the absence of a magnetic field.

In the presence of a magnetic field the local field orientation defines a quantization axis. In fig. 5.6 we have given some examples of how the magnetic field determines the quantization axis. The unprimed axis define the lab frame, the atom frame is marked by primed coordinates. In figure (a) the magnetic field points along

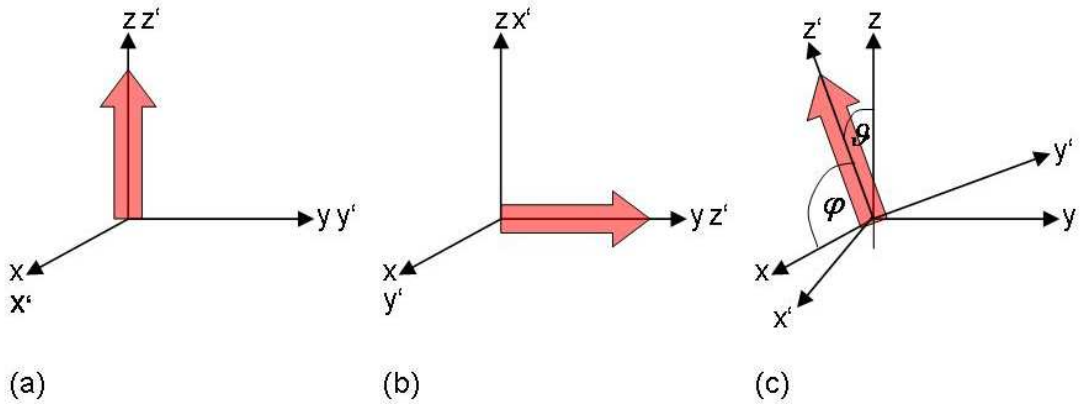

Figure 5.6: Definition of the quantization axis by an external magnetic field. The direction of the magnetic field is represented by the red arrow. Unprimed coordinates belong to the lab frame, coordinates in the atom frame are primed.

the $\hat{z}$-axis of the lab frame. The quantization axis $\hat{z}'$ corresponds to the $\hat{z}$-axis in the lab frame. This causes the atoms to view the $\{\hat{x}, \hat{y}\}$ polarization of the Raman beams the same as in the lab frame. Hence the coupling to the state $|f\rangle$ is governed by $\Delta m = 0$ transitions. If the magnetic field points along one of the polarization axis, for example along the $\hat{y}$-axis as in (b), the polarization in the atom frame is $\{\hat{y}', \hat{z}'\}$. This configuration therefore leads to $\Delta m = \pm 1$ transitions. Generally the magnetic field can point in an arbitrary direction (c). This corresponds to a linear combination of the two cases discussed before and transitions with $\Delta m = 0$ and $\Delta m = \pm 1$ happen.

All our calculations will be done in the lab frame, where the Raman beam po-

larizations stay constant, while the quantization axis rotates according to the magnetic field orientation. The rotation angles, as they are defined in fig. 5.6 (c), are given by

$$sin\ \theta(\vec{r}) = \frac{\sqrt{B_x^2(\vec{r}) + B_y^2(\vec{r})}}{\sqrt{B_x^2(\vec{r}) + B_y^2(\vec{r}) + B_z^2(\vec{r})}} \tag{5.35}$$

$$cos\ \theta(\vec{r}) = \frac{B_z(\vec{r})}{\sqrt{B_x^2(\vec{r}) + B_y^2(\vec{r}) + B_z^2(\vec{r})}} \tag{5.36}$$

$$sin\ \phi(\vec{r}) = \frac{B_x(\vec{r})}{\sqrt{B_x^2(\vec{r}) + B_y^2(\vec{r})}} \tag{5.37}$$

$$cos\ \phi(\vec{r}) = \frac{B_y(\vec{r})}{\sqrt{B_x^2(\vec{r}) + B_y^2(\vec{r})}}. \tag{5.38}$$

Thus we are able to determine the effective Raman-Rabi frequencies $\beta_{i,0}$ in the atom frame by rotating the Raman transition operator. For further calculations it is useful to go back to the spherical tensor notation, T(k,q). k describes the rank of the operator, q the $\hat{z}$ component of the operators angular momentum.

We can define $\beta_{0,0} = T(1,0)$. In the absence of a magnetic field, the transition operator T(1,0) corresponds to $\Delta m = 0$ transitions. In the rotated frame this tensor becomes

$$T(1,0) = \sum_q D^1_{q0}(\vec{r})\ T'(1,q), \tag{5.39}$$

where $D^1_{q0}(\vec{r})$ are the Wigner rotation matrix elements which can be expressed using the spherical harmonics $Y_{1q}(\theta(\vec{r}), \phi(\vec{r}))$,

$$D^1_{q0}(\vec{r}) = (-1)^q \sqrt{\frac{4\pi}{3}} Y_{1q}(\theta(\vec{r}).\phi(\vec{r})), \tag{5.40}$$

The angles θ and ϕ describe the rotation of the quantization axis.

The relation between the spherical tensor operator in the lab and the rotated

frame is obtained by expanding the sum,

$$T(1,0) = T'(1,0)\ cos\ \theta(\vec{r}) + \frac{1}{\sqrt{2}}T'(1,-1)\ sin\ \theta(\vec{r})\ e^{-i\phi(\vec{r})} + \frac{1}{\sqrt{2}}T'(1,1)\ sin\ \theta(\vec{r})\ e^{i\phi(\vec{r})}. \quad (5.41)$$

This has to be true for all angles θ and ϕ. By choosing $\theta = \phi = 0$ we therefore find that

$$T(1,0) = T'(1,0) = \beta_{0,0}. \quad (5.42)$$

We will use the Wigner-Eckart Theorem to determine the remaining effective Raman-Rabi frequencies in the rotated frame; using eq. A.6 we find them to be

$$\beta_{-1,0} = \beta_{1,0} = \frac{1}{2}\beta_{0,0}. \quad (5.43)$$

After doing the transformation to the lab frame using eq. 5.41 the Raman-Rabi frequency become

$$\beta_{0,0}(\vec{r}) = T'(1,0)\ cos\ \theta(\vec{r}) = \beta_{0,0}\ cos\ \theta(\vec{r}) \quad (5.44)$$

$$\beta_{-1,0}(\vec{r}) = \frac{1}{\sqrt{2}}T'(1,-1)\ sin\ \theta(\vec{r}) = \frac{1}{2\sqrt{2}}\beta_{0,0}\ sin\ \theta(\vec{r}) \quad (5.45)$$

$$\beta_{1,0}(\vec{r}) = \frac{1}{\sqrt{2}}T'(1,1)\ sin\ \theta(\vec{r}) = \frac{1}{2\sqrt{2}}\beta_{0,0}\ sin\ \theta(\vec{r}). \quad (5.46)$$

We have neglected phase information in these expressions since only the magnitude of the Raman-Rabi frequencies matters for the final state probability. The remaining Raman-Rabi frequencies of the initial states with magnetic quantum number $m = \pm 1$ can be treated similarly.

The final state probability can therefore be determined by adding the contributions from all initially populated states. The transfer efficiency is determined by the product of the effective Raman-Rabi frequency and the pulse duration, while the product of the detuning from resonance due to a magnetic field gradient and the pulse duration determines the resolution. The *magnitude* of the external magnetic field influences the effective detuning ($\delta - \delta_i^B(\vec{r})$), while the *direction* affects the effective Raman-Rabi frequency β.

Chapter 6

Raman transitions of Sodium atoms

The following chapter uses the theory for stimulated Raman transitions we described previously to calculate the ideal pulse duration needed to ensure a complete population transfer from the $|F = 1\rangle$ to the $|F = 2\rangle$ ground state in Sodium. Furthermore, we determine the spatial resolution achieved by applying a magnetic field gradient and propose an experimental method to determine the pulse duration and the magnetic field dependance.

6.1 Magnetic detuning from Raman Resonance

In section 5.5 we already introduced the detuning $\delta^B_{m_f,m_i}(\vec{r}) = \frac{\gamma_{m_f,m_i}\mu_B}{\hbar}B(\vec{r})$ due to the magnetic field. We will now calculate this detuning for Sodium atoms. Knowing the Landé-g-factors for the ground state of Sodium, $g_i = -1/2$ (F=1) and $g_f = +1/2$ (F=2), we can calculate γ_{m_f,m_i}. The numerical values are shown in table 6.1. With these values we can now calculate $\delta^B_{m_f,m_i}(\vec{r})$ for some particular initial and final state combination.

6.2 Dipole matrix elements

Before we can calculate the effective Raman-Rabi frequencies we need to determine the transition dipole matrix elements $\langle J = 1/2||\mu||J = 3/2\rangle$ and $\langle J = 1/2||\mu||J = 1/2\rangle$. In

	$m_{final} = -2$	$m_{final} = -1$	$m_{final} = 0$	$m_{final} = 1$	$m_{final} = 2$
$m_{initial} = -1$	-3/2	-1	-1/2	0	1/2
$m_{initial} = 0$	-1	-1/2	0	1/2	1
$m_{initial} = 1$	-1/2	0	1/2	1	3/2

Table 6.1: Calculation of γ_{m_f,m_i} in Sodium for the $|F = 1\rangle \rightarrow |F' = 2\rangle$-Raman transition

section 2.4 we already used the relation between the transition dipole matrix element and the lifetime of the respective transition. Knowing the lifetime of the $3^2P_{3/2}$ and the $3^2P_{1/2}$ excited state we can calculate the dipole matrix elements using [10]

$$|\langle J'||e\vec{r}||J\rangle| = \sqrt{\frac{1}{\tau_{J'J}}\frac{3\pi\epsilon_0\hbar\lambda^3}{(2\pi)^3}(2J'+1)}. \tag{6.1}$$

The dipole matrix elements for the D_2- and D_1-line are

$$|\langle J = 1/2||\mu||J = 3/2\rangle| = 4.22 \cdot 10^{-29} Cm \tag{6.2}$$

and

$$|\langle J = 1/2||\mu||J = 1/2\rangle| = 2.11 \cdot 10^{-29} Cm \tag{6.3}$$

respectively.

6.3 Effective Raman-Rabi frequencies and final state probability

In a multi-level atom the effective Raman-Rabi frequency is given by

$$\beta_{fi} = -\sum_I \frac{\langle f|\vec{\mu}\vec{E}_2|I\rangle\langle I|\vec{\mu}\vec{E}_1|i\rangle}{2\hbar^2\Delta_I}, \tag{6.4}$$

where we have to sum over all possible paths for a transition, see section 5.4.1.

In this section we will assume without loss of generality that the two electric fields are $\{\hat{y}, \hat{z}\}$ linearly polarized or $\vec{E}_1 = E_1\hat{y}$, $\vec{E}_2 = E_2\hat{z}$. The magnetic field is taken to

be in the $\hat{z}$-direction, $\vec{B} = B\hat{z}$.

The quantization axis of the atom is defined by the external magnetic field. Hence in the atom frame we can expand the linear (π) polarized field in the $\hat{y}$-direction into two circular polarized ($\sigma^+ + \sigma^-$) fields. These lead to transitions with a change of $\Delta m = \pm 1$ in the magnetic quantum number. While the expansion is possible in $\hat{y}$-direction it is impossible in $\hat{z}$-direction, which coincides with the quantization axis.

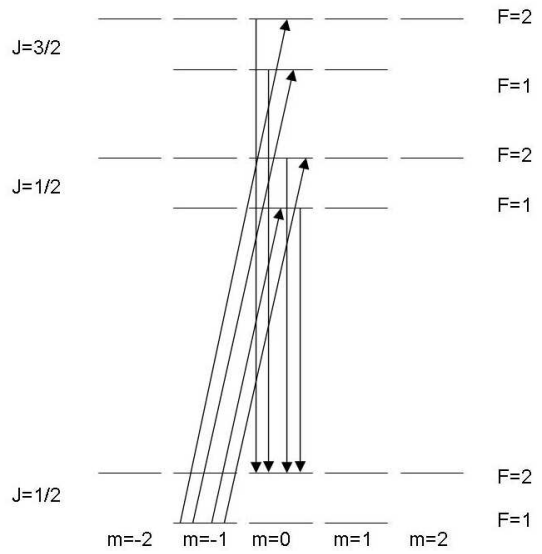

Figure 6.1: Schematic of the possible Raman transitions leading to the effective Raman-Rabi frequency β_{0-1}

In this configuration it is simple to identify the possible paths leading to the transition $|F = 1, m = -1\rangle \rightarrow |F = 2, m = 0\rangle$ which are schematically shown in fig. 6.1. Hence we can calculate the effective Raman-Rabi frequency β_{0-1} by adding the individual Raman-Rabi frequencies of each path,

$$
\begin{aligned}
\beta_{0-1} &= -\sum_I \frac{\langle F=2,m=0|\vec{\mu}\vec{E}_2|I\rangle\langle I|\vec{\mu}\vec{E}_1|F=1,m=-1\rangle}{2\hbar^2\Delta_I} \\
&= -\frac{1}{\sqrt{2}}\frac{E_1E_2}{2\hbar^2}\sum_I \frac{\langle F=2,m=0|\mu_2|I\rangle\langle I|\mu_1|F=1,m=-1\rangle}{2\hbar^2\Delta_I} \\
&= -\frac{1}{\sqrt{2}}\frac{E_1E_2}{2\hbar^2}\Big(\frac{1}{\Delta_{3/2}}\langle F=2,m=0|\mu_2|F=1,m=0\rangle\langle F=1,m=0|\mu_1|F=1,m=-1\rangle \\
&\quad +\frac{1}{\Delta_{3/2}}\langle F=2,m=0|\mu_2|F=2,m=0\rangle\langle F=2,m=0|\mu_1|F=1,m=-1\rangle \\
&\quad +\frac{1}{\Delta_{1/2}}\langle F=2,m=0|\mu_2|F=1,m=0\rangle\langle F=1,m=0|\mu_1|F=1,m=-1\rangle \\
&\quad +\frac{1}{\Delta_{1/2}}\langle F=2,m=0|\mu_2|F=2,m=0\rangle\langle F=2,m=0|\mu_1|F=1,m=-1\rangle\Big) \\
&= -\frac{1}{\sqrt{2}}\frac{E_1E_2}{2\hbar^2}\Big(\frac{1}{\Delta_{3/2}}\sqrt{\frac{1}{60}}\sqrt{\frac{5}{48}}\cdot(4.22\cdot10^{-29}Cm)^2+\frac{1}{\Delta_{3/2}}0\sqrt{\frac{1}{48}}\cdot(4.22\cdot10^{-29}Cm)^2 \\
&\quad +\frac{1}{\Delta_{1/2}}\sqrt{\frac{1}{6}}\sqrt{-\frac{1}{24}}\cdot(2.11\cdot10^{-29}Cm)^2+\frac{1}{\Delta_{1/2}}0\sqrt{-\frac{1}{24}}\cdot(2.11\cdot10^{-29}Cm)^2\Big) \\
&= -\frac{1}{\sqrt{2}}\frac{E_1E_2}{2\hbar^2}\cdot1.09\cdot10^{-73}C^2m^2. \qquad (6.5)
\end{aligned}
$$

The detunings $\Delta_{1/2}$ and $\Delta_{3/2}$ are the detunings of a Verdi laser beam (532nm) from the D_1- and D_2-line respectively. The detunings due to the hyperfine splitting of the excited states are negligible. We should keep in mind that E_1 and E_2 cannot be chosen independantly. The theoretical description for the final state probability is only valid if the relative light shifts between the two ground states vanishes. In Sodium we will introduce an undesired AC-Stark shift if $E_1 \neq E_2$.

It is sufficient to calculate one Raman-Rabi frequency explicitly, the others can be calculated using the Wigner-Eckart Theorem, e.g.

$$
\begin{aligned}
\beta_{00} &= \langle F=2,m=0|\mu|F=1,m=0\rangle = (-1)^2\begin{pmatrix}2&1&1\\0&0&0\end{pmatrix}\langle F=2||\mu||F=1\rangle \\
&= \sqrt{\frac{2}{15}}\sqrt{30}\,\beta_{0-1} = 2\,\beta_{0-1} \qquad (6.6)
\end{aligned}
$$

The values for the effective Raman-Rabi frequencies are listed in tab. 6.2 as multiples of β_{00}.

With the calculation of the detuning from the Raman resonance and the effective Raman-Rabi frequency we are now able to write down an expression for the final state probability, depending on position $\vec{r}$, Raman detuning δ and pulse duration τ

$$\begin{aligned}
P_f(r,\theta,\delta,\tau) &= \frac{1}{3}\,(sin^2\,(\frac{\sqrt{3}}{4}\,\tau\,\beta_{00}\,sin\,\theta)\cdot \\
&\quad (sinc^2(\frac{(\delta+3/2\,\mu_B\,dB/dr\cdot r/\hbar)\,\tau}{2})+sinc^2(\frac{(\delta-3/2\,\mu_B\,dB/dr\cdot r/\hbar)\,\tau}{2})) \\
&\quad +sin^2\,(\frac{\sqrt{3}}{4}\,\tau\,\beta_{00}\,cos\,\theta)\cdot \\
&\quad (sinc^2(\frac{(\delta+\mu_B\,dB/dr\cdot r/\hbar)\,\tau}{2})+sinc^2(\frac{(\delta-\mu_B\,dB/dr\cdot r/\hbar)\,\tau}{2})) \\
&\quad +sin^2\,(\frac{1}{\sqrt{2}4}\,\tau\,\beta_{00}\,sin\,\theta)\cdot \\
&\quad (sinc^2(\frac{(\delta+1/2\,\mu_B\,dB/dr\cdot r/\hbar)\,\tau}{2})+sinc^2(\frac{(\delta-1/2\,\mu_B\,dB/dr\cdot r/\hbar)\,\tau}{2})) \\
&\quad +sin^2\,(\frac{\sqrt{3}}{\sqrt{2}4}\,\tau\,\beta_{00}\,sin\,\theta)\cdot \\
&\quad (sinc^2(\frac{(\delta+1/2\,\mu_B\,dB/dr\cdot r/\hbar)\,\tau}{2})+sinc^2(\frac{(\delta-1/2\,\mu_B\,dB/dr\cdot r/\hbar)\,\tau}{2})) \\
&\quad +sin^2\,(\frac{1}{2}\,\tau\,\beta_{00}\,cos\,\theta)\cdot sinc^2(\frac{\delta\,\tau}{2})). \qquad (6.7)
\end{aligned}$$

	$m_{final}=-2$	$m_{final}=-1$	$m_{final}=0$	$m_{final}=1$	$m_{final}=2$
$m_{initial}=-1$	$\frac{\sqrt{3}}{2}\,sin\,\theta$	$\frac{\sqrt{3}}{2}\,cos\,\theta$	$\frac{1}{2}\sqrt{2}\,sin\,\theta$		
$m_{initial}=0$		$\frac{\sqrt{3}}{2}\sqrt{2}\,sin\,\theta$	$cos\,\theta$	$\frac{\sqrt{3}}{2}\sqrt{2}\,sin\,\theta$	
$m_{initial}=1$			$\frac{1}{2}\sqrt{2}\,sin\,\theta$	$\frac{\sqrt{3}}{2}\,cos\,\theta$	$\frac{\sqrt{3}}{2}\,sin\,\theta$

Table 6.2: Calculation of the effective Raman-Rabi frequencies in the lab frame; in multiples of $\beta_{0,0}$. θ is defined as in eqs. 5.35 and 5.36

6.4 Numerical results for Sodium atoms

Before we can calculate the spatial resolution we need to find the optimal pulse duration to ensure a complete transfer of atoms from the $|F=1\rangle$ to the $|F=2\rangle$ state. We therefore ignore , for the time being, the effects due to the detuning from the Raman resonance frequency and an external magnetic field and concentrate on the time development.

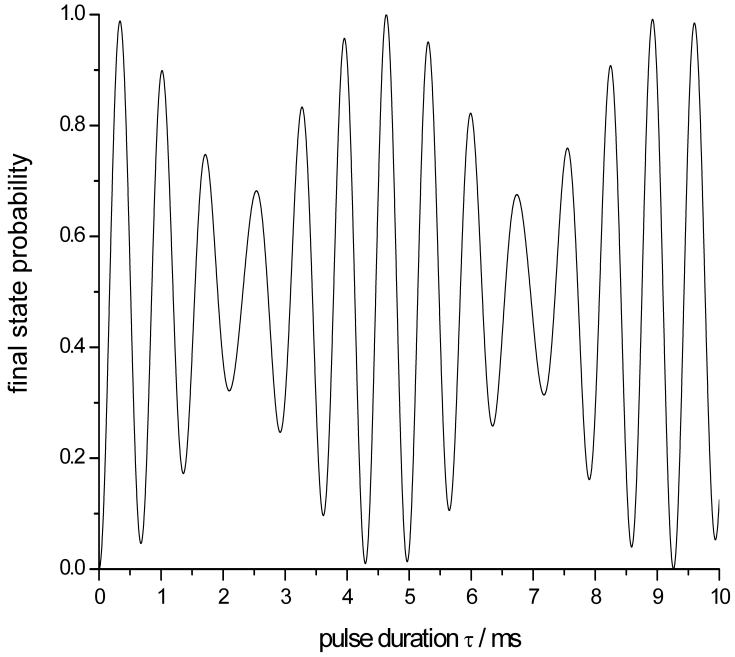

Figure 6.2: Dependance of the final state probability of pulse duration τ.

In a future experimental setup, the detuning between the two Raman beams will be created by an Acousto-Optic Frequency Shifter (Brimrose TEF-1700-350-589) with an optical threshold of $100W/mm^2$ and a diffraction efficiency of 14.8% at a wavelength of 532nm. The time development of the final state probability depends critically on the intensities of the two Raman beams. So it is important to note that the following calculations are based on beams with 7.6 mW with a beam waist of $50\mu m$. The large beam waist guarantees that the intensity in the Raman resonance region is approximately constant. A plot of the time dependance is shown in fig. 6.2. After a pulse duration of $337.3\mu s$ the population transfer reaches 98.8%.

With a pulse of length $337.3\mu s$, less than 20kHz detuning from the Raman resonance frequency will reduce the population transfer significantly, as can be seen in fig. 6.3. This results in a spectral resolution of less than $250nm$ if we take the magnetic field gradient to be $150G/cm$. Nevertheless, the spatial resolution is severely limited due to the initial velocity of the atoms and their acceleration during the Raman pulse.

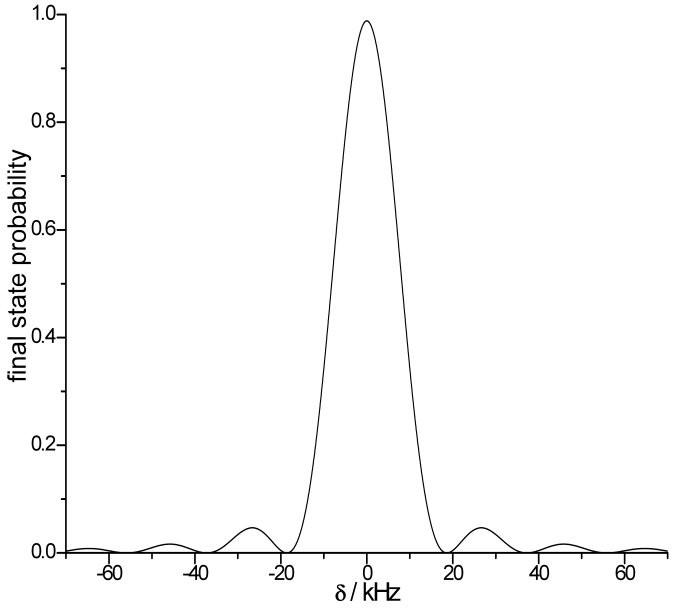

Figure 6.3: Dependance of the final state probability of the detuning δ from the Raman resonance frequency

By confining the atoms in an optical lattice it is possible to circumvent the resolution limits due to the atoms velocity and acceleration. We can then use a long pulse duration time, to ensure an efficient population transfer and to gain a good spectral resolution. But this also means that the resolution is ultimately limited by the size of each individual lattice site, i.e. 266nm for a beam with a wavelength of 532nm. The center of the resonant Raman region should coincide with the center of the lattice site to avoid a population transfer in the two neighbouring sites.

A magnetic field gradient of $150G/cm$ means a splitting of the magnetic levels according to the anomalous Zeeman effect. Fig. 6.4 represents the case where the quantization axis of the atoms coincides with the z-direction in the lab frame (magnetic field along the direction of beam propagation). In this case eq. 6.7 reduces to

$$
\begin{aligned}
P_f(r,\theta,\delta,\tau) &= \frac{1}{3}\,(sin^2\,(\frac{\sqrt{3}}{4}\,\tau\,\beta_{00}\,)\cdot \\
&\quad (sinc^2(\frac{(\delta+\mu_B\,dB/dr\cdot r/\hbar)\,\tau}{2}) + sinc^2(\frac{(\delta-\mu_B\,dB/dr\cdot r/\hbar)\,\tau}{2})) \\
&\quad +sin^2\,(\frac{1}{2}\,\tau\,\beta_{00}\,)\cdot sinc^2(\frac{\delta\,\tau}{2})).
\end{aligned}
\tag{6.8}
$$

Since one third of the transitions are insensitive to a change in the magnetic field, at least one third of the initial population of the $|F=1\rangle$ state will be transferred to the $|F=2\rangle$ state, while in the resonant Raman region up to 98.8% can be transferred. This behaviour is shown in fig. 6.4.

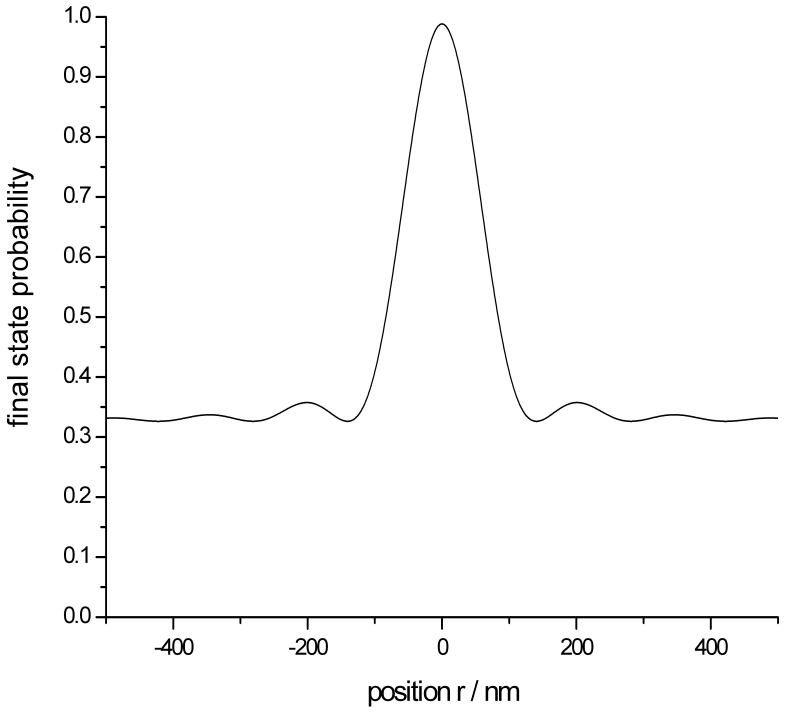

Figure 6.4: The final state probability as a function of the position. 0 belongs to the point of 0 magnetic field. The Raman detuning δ equals 0, the magnetic field gradient is 150G/cm. The angle θ equals 0, i.e. the magnetic field points along the z-axis (atom and lab frame coincide).

In the absence of a magnetic field, all sublevels are equally populated. In a magnetic trap only the atoms with F=1 M=-1 will be trapped. In this case eq. 6.7 reduces to

$$\begin{aligned} P_f(r,\theta,\delta,\tau) &= sin^2\left(\frac{\sqrt{3}}{4}\tau\beta_{00}\sin\theta\right)\cdot sinc^2\left(\frac{(\delta+3/2\,\mu_B\,dB/dr\cdot r/\hbar)\,\tau}{2}\right) \\ &\quad +sin^2\left(\frac{\sqrt{3}}{4}\tau\beta_{00}\cos\theta\right)\cdot sinc^2\left(\frac{(\delta+\mu_B\,dB/dr\cdot r/\hbar)\,\tau}{2}\right) \\ &\quad +sin^2\left(\frac{1}{\sqrt{2}4}\tau\beta_{00}\sin\theta\right)\cdot sinc^2\left(\frac{(\delta+1/2\,\mu_B\,dB/dr\cdot r/\hbar)\,\tau}{2}\right). \end{aligned} \quad (6.9)$$

A plot of the final state probability as a function of the position $\vec{r}$ is shown in fig. 6.5. The optimal pulse duration changes to 345.0μs and the population transfer reaches 100%, since the resonance frequency of the transition from the M=-1 level is dependant on the magnetic field. Therefore only atoms in the resonant Raman region can be transferred.

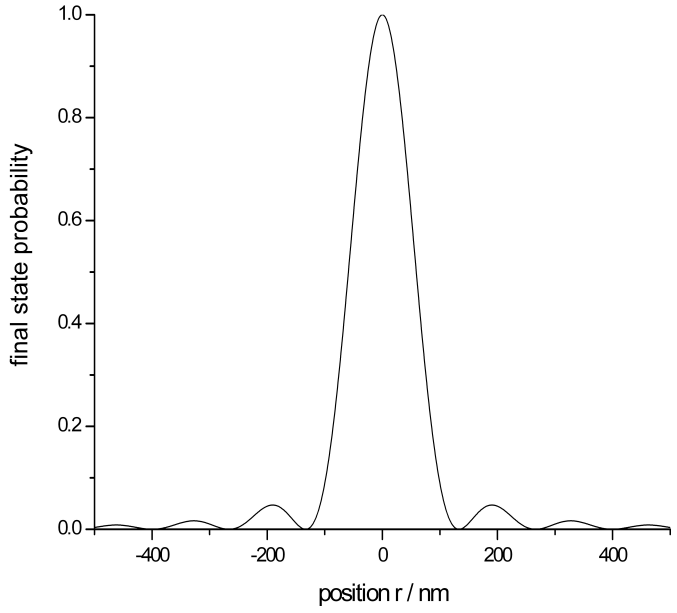

Figure 6.5: Dependance of the final state probability of the position. O belongs to the point of 0 magnetic field. The Raman detuning δ equals 0, the magnetic field gradient is 150G/cm. The angle θ equals 0, i.e. the magnetic field points along the z-axis (atom and lab frame coincide). All atoms start in the F=1 M=-1 state.

In all the calculations done above we have assumed the Raman detuning δ to be zero, i.e. the difference frequency equals the hyperfine splitting of the Sodium ground states in absence of a magnetic field (1.772GHz). By changing the detuning we can vary the position of the resonant Raman region in space. A detuning of 1MHz corresponds to a spatial shift of the resonant region by 7.55 μm.

6.5 Experimental procedure to determine the transfer efficiency of stimulated Raman transitions

The experimental procedure used to test the efficiency of the Raman pulse is rather simple. After loading the MOT and cooling the trapped atoms, the repump beam is turned off. Therefore atoms that fall into the $|F = 1\rangle$ state remain there and are separated from the $|F = 2\rangle \rightarrow |F' = 3\rangle$ cycling transition. Eventually all atoms will fall into this dark state. The atoms can then be transferred into the magnetic trap. In the future, the trap will be in an Anti-Helmholtz configuration with an optical plug [31]. In this trap only the atoms with the magnetic sublevel M=-1 will be trapped. An evaporation cooling technique is then used to create a Bose Einstein Condensate. The optical lattice is created next and the atoms are confined to individual lattice sites.

A Raman pulse is then applied and the corresponding number of atoms make the transition to the $|F = 2\rangle$ state. The resonant light is turned on. Although the resonant light forms a closed transition all atoms will eventually fall in the $|F = 1\rangle$ state again after a certain number of cycling transitions. During this process they gain energy and a time-of-flight measurement could separate the two atom groups and the atom number of those that made the Raman transition can be determined. Knowledge of the initial number of atoms is a crucial element of determining the Raman transition efficiency. One therefore must be certain that the initial number of atoms does not vary by more than a few percent.

Knowing the ideal pulse duration one can study the population transfer efficiency as a function of a magnetic bias field. The relation between those two can then be

used to determine the necessary magnetic field gradient to achieve the desired spatial resolution.

Instead of using a time-of-flight measurement one could also think of lowering the depth of the optical lattice. The atoms that underwent the Raman transition and therefore the cycling transition will leave the trap before the other atoms do which did not make the Raman transition. It is then possible to determine the atom number of the remaining atoms.

In the proposed configuration for spatially resolved Raman imaging the magnetic field gradient is along the propagation axis of the two co-propagating Raman beams which are linearly polarized in $\hat{x}$- and $\hat{y}$-direction respectively. By preparing all atoms to be in the $|F = 1, M = -1\rangle$ state and confining them in an optical lattice a spatial resolution of one lattice site seems achievable applying a magnetic field gradient of 150 G/cm. A change in the Raman detuning can be used to vary the resonant Raman region in space. The resonant Raman region is at the point of zero magnetic field if the difference frequency equals the hyperfine splitting in absence of a magnetic field (1.772GHz).

Appendix A

Wigner-Eckart Theorem

When dealing with different angular momenta, their couplings, and transition probabilities, it can be very helpful to use the Wigner-Eckart Theorem. It allows a separation of a matrix element $\langle \alpha' j' m' | T(k,q) | \alpha j m \rangle$ into a scalar matrix element (reduced matrix element) $\langle \alpha' j' || T^k || \alpha j \rangle$, which carries the information about the dynamics of the system, and a Wigner-3j-symbol (Clebsch-Gordan coefficient), that carries the geometrical and symmetrical properties. The Wigner-3j-symbol therefore includes the selection rules for radiative transitions.

We will follow the proofs given by Zare [12] and Edmonds [32] and consider first a rotation of the state vector $T(k,q)|\alpha' j' m'\rangle$,

$$\begin{aligned} \mathbf{R}\left[T(k,q)\,|\alpha' j' m'\rangle\right] &= \mathbf{R}\,T(k,q)\,\mathbf{R^{-1}}\,\mathbf{R}\,|\alpha' j' m'\rangle \\ &= \sum_{q',m''} D^{k}_{q'q}(R)\, D^{j'}_{m''m'}(R)\,[T(k,q')|\alpha' j' m''\rangle] \\ &= \sum_{q',m''} \mathbf{D^{k}} \otimes \mathbf{D^{j'}}\,[T(k,q')|\alpha' j' m''\rangle, \end{aligned} \tag{A.1}$$

where $D^{l}_{m'm}(R)$ are the Wigner rotation matrix elements. These can be expressed by spherical harmonics $\mathtt{Y}_{1,q}$

$$D^{1}_{q,0}(\vec{r}) = (-1)^{q} \left(\frac{4\pi}{3}\right)^{1/2} \mathtt{Y}_{1,q}(\theta(\vec{r}), \phi(\vec{r})). \tag{A.2}$$

The product of the two rotation matrices $\mathbf{D^k} \otimes \mathbf{D^{j'}}$ in eq. A.1 can be expressed as a product of Clebsch-Gordan coefficients and a rotation matrix $\mathbf{D^K}$. The linear combination of the products $T(k,q')|\alpha' j' m''\rangle$, that transforms under rotation as a particular state $|\beta KQ\rangle$ of the basis functions of the rotation matrix $\mathbf{D^k}$ is

$$|\beta KQ\rangle = \sum_{q,m''} \langle kq', j'm''|KQ\rangle T(k,q')|\alpha' j' m''\rangle, \tag{A.3}$$

where $\langle kq', j'm''|KQ\rangle$ is a Clebsch-Gordan coefficient. Taking the inner product with $\langle \alpha jm|$

$$\sum_{q,m''} \langle kq', j'm''|KQ\rangle \langle \alpha jm|T(k,q')|\alpha' j' m''\rangle = \langle \alpha jm|\beta KQ\rangle \tag{A.4}$$

can further be manipulated by multiplying both sides with $\langle kq, j'm'|KQ\rangle$ and doing the summation over K and Q. The inner product $\langle \alpha jm|\beta jm\rangle$ equals the reduced matrix element $\langle \alpha j||T_k||\alpha' j'\rangle$, and the scalar product $\langle \alpha jm|\beta KQ\rangle$ vanishes unless $j = K$ and $m = Q$.

$$\begin{aligned} \langle \alpha jm|T(k,q')|\alpha' j' m'\rangle &= \sum_{KQ} \langle \alpha jm|\beta KQ\rangle \langle kq, j'm'|KQ\rangle \\ &= \langle kq, j'm'|jm\rangle \langle \alpha j||T_k||\alpha' j'\rangle. \end{aligned} \tag{A.5}$$

Hence we have successfully separated the dynamics from the geometrical properties of the system.

By transforming the Clebsch-Gordan coefficients of eq. A.5 into Wigner-3j-symbols we derive the Wigner-Eckart Theorem in the form used in this thesis,

$$\langle \alpha jm|T(k,q')|\alpha' j' m'\rangle = (-1)^{j-m} \begin{pmatrix} j & k & k' \\ -m & q & m' \end{pmatrix} \langle \alpha j||T^k||\alpha' j'\rangle. \tag{A.6}$$

One should be careful with the conventions of the reduced matrix elements. We have adopt the convention of Zare [12] and Edmonds [32], while others, e.g. Brink [33], define the reduced matrix element by a factor of $\frac{1}{\sqrt{2j+1}}$ smaller.

Appendix B

Properties of Sodium

In this appendix we want to give a brief overview of the physical properties of Sodium and the essential experimental parameters as far as they are needed in the context of this thesis.

B.1 General properties

Sodium has one unpaired electron in the valence orbital, as all alkali atoms do. A quantum mechanical description of a Sodium atom can be found by starting with a hydrogen-like atom denoted by the state $|nlm_l\rangle$, where n is the principal quantum number, l is the angular momentum quantum number and m_l the magnetic quantum number. The valence electron is in a spin state $|sm_s\rangle$. A coupling of the Spin $\vec{S}$ to the angular momentum $\vec{L}$ leads to the total angular momentum $\vec{J} = \vec{L} + \vec{S}$. Furthermore a coupling to the nuclear spin $\vec{I}$ leads to a total angular momentum of $\vec{F} = \vec{J} + \vec{I}$. The state of the atom is then described by $|\alpha F m_F\rangle$, where α stands for all quantum numbers that are not written explicitly, and $|F| = |I - J|, ..., |I + J|$, $m_F = -F, ..., F$. In the absence of a magnetic field, magnetic sublevels with the same value of F are degenerate.

A grotrian diagram of Sodium, neglecting fine and hyperfine splittings, is shown in fig. B.1. A simple energy level diagram for the ground state and the first excited state, including fine and hyperfine splittings as well as the magnetic splitting in agreement

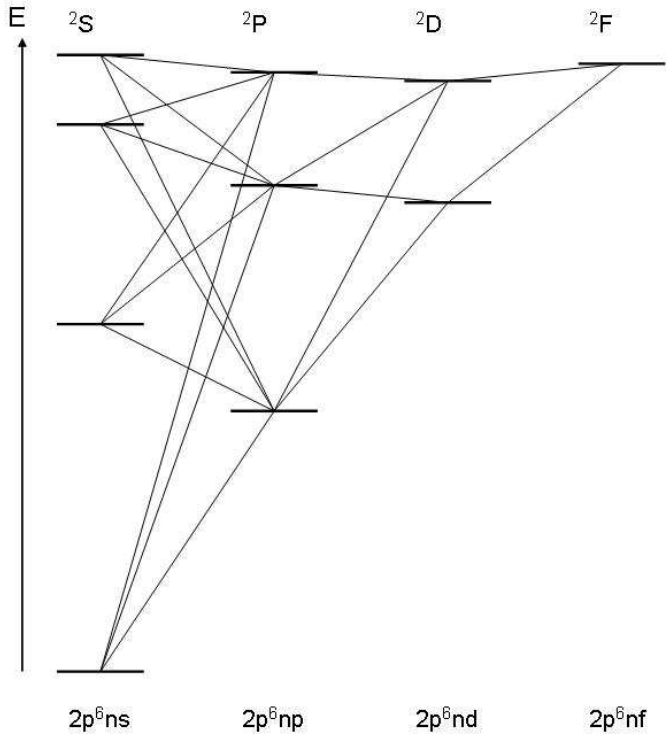

Figure B.1: Grotrian diagram for Sodium, neglecting fine and hyperfine structure splittings. Allowed transitions are indicated. The spectroscopic notation and the atomic configuration are presented. Energy is not to scale.

with the anomalous Zeeman effect, is shown in fig. B.2.

The slowing transition for the Zeeman-slower is 20MHz red detuned from the $|F = 2\rangle \rightarrow |F' = 3\rangle$-transition. Eventually the atoms will leave the cycling-transition used to slow and cool them, and will fall into the dark state (F=1). The repump beam between the $|F = 1\rangle \rightarrow |F' = 2\rangle$-transition pumps the atom back into the cycling-transition, see fig. B.3.

In table B.1 we have summarized some basic physical properties.

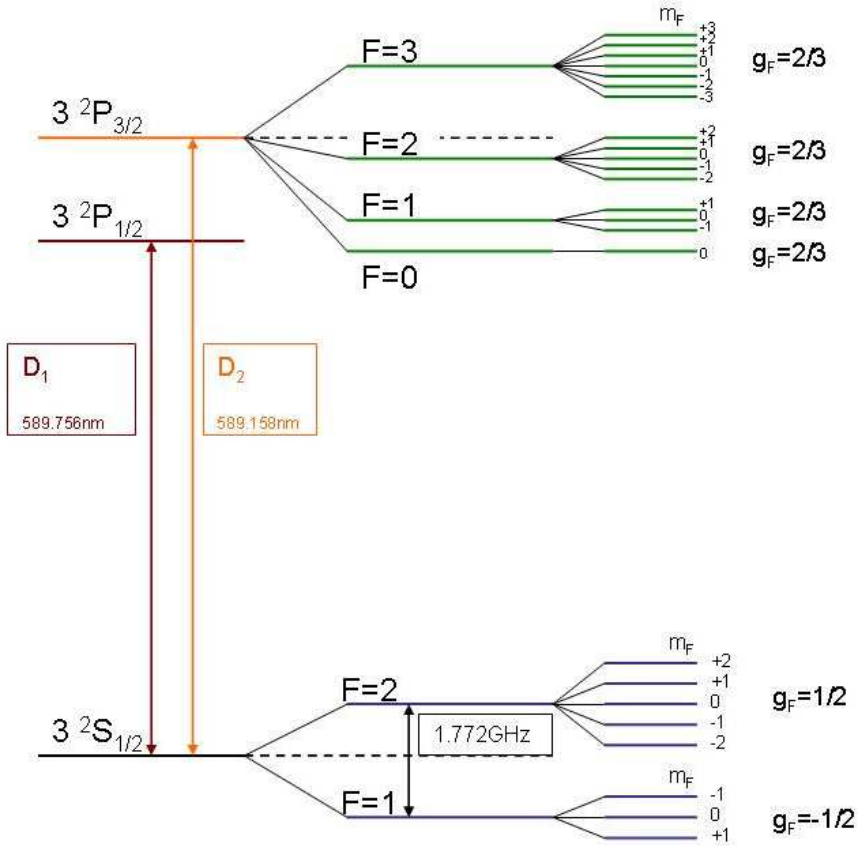

Figure B.2: Schematic of the ground state and the first excited state energy level. The hyperfine splitting is indicated for the $3^2S_{1/2}$ ground state and the $3^2P_{3/2}$ state. The magnetic splitting is according to the anomalous Zeeman effect. The wavelengths for the resonant transitions are presented, as are the Landé-g-factors. Energy is not to scale.

B.2 Sodium in an external magnetic field

The degeneracy of the (2F+1) magnetic levels breaks down in an external magnetic field. If we take the magnetic field to be along the atomic quantization axis (z-axis), the Hamiltonian

$$H_B = \frac{\mu_B}{\hbar}\left(g_S S_z + g_L L_z + g_I I_z\right) B_z \tag{B.1}$$

describes the interaction of the atom with the magnetic field. g_S, g_L and g_I are the Landé-g-factors for the electron spin, electron orbital and nuclear spin respectively [20]. If hyperfine splittings are important, F is a good quantum number, and the

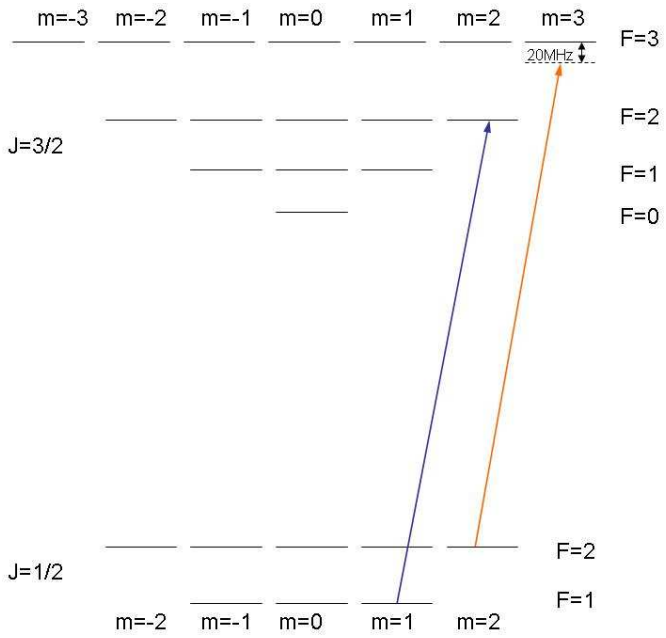

Figure B.3: Schematic of the cycling transition $F = 2 \rightarrow F' = 3$ with the red detuned beam (orange) and the repump beam (blue). Energy is not to scale.

interaction Hamiltonian becomes

$$H_B = \mu_B g_F F_z B_z. \tag{B.2}$$

In a weak external magnetic field the magnetic levels split according to the anomalous Zeeman effect. The perturbation of the interaction Hamiltonian to the zero field eigenstates is, to lowest order, given by

$$\Delta E = \mu_B g_F m_F B_z, \tag{B.3}$$

where

$$g_F \approx g_J \frac{F(F+1) - I(I+1) + J(J+1)}{2F(F+1)}. \tag{B.4}$$

atomic number	Z	11
number of nucleons	Z+N	23
relative natural abundance	$\eta(^{23}Na)$	100%
nuclear spin	I	3/2
D_2-line frequency	ω	$2\pi\cdot$ 508.8487162(13)THz
D_2-line lifetime	τ	16.249(19)ns
D_1-line frequency	ω	$2\pi\cdot$ 508.3324657(13)THz
D_1-line lifetime	τ	16.299(21)ns
Landé-g-factor g_J	$3^2S_{1/2}$	2.0022969(7)
Landé-g-factor g_J	$3^2P_{1/2}$	0.66581(12)
Landé-g-factor g_J	$3^2P_{3/2}$	1.332(2)

Table B.1: Physical properties of Sodium atoms [20]

For high magnetic fields, the levels split according to the Paschen-Back-effect

$$\Delta E = A_{hfs} m_J m_I + B_{hfs} \frac{3(m_J m_I)^2 + \frac{3}{2} m_J m_I - I(I+1)J(J+1)}{2J(2J-1)I(2I-1)} + \mu_B (g_J m_J + g_I m_I) B_z, \quad \text{(B.5)}$$

where A_{hfs} and B_{hfs} are hyperfine structure constants.

For intermediate magnetic fields the splitting is in general difficult to calculate, but if either $J = 1/2$ or $I = 1/2$ an analytic description is given by the Breit-Rabi-formula. For the ground state manifold in Sodium the Breit-Rabi-formula is

$$\Delta E = -\frac{A_{hfs}(I+1/2)}{2(2I+1)} + g_I \mu_B m B \pm \frac{A_{hfs}(I+1/2)}{2} \left(1 + \frac{4mx}{2I+1} + x^2\right)^{1/2}, \quad \text{(B.6)}$$

with $m = m_I \pm m_J$ (sign to be taken as in eq. B.6) and

$$x = \frac{(g_J - g_I)\mu_B B}{A_{hfs}(I+1/2)}. \quad \text{(B.7)}$$

Fig. B.4 shows the magnetic field dependance of the ground state manifold.

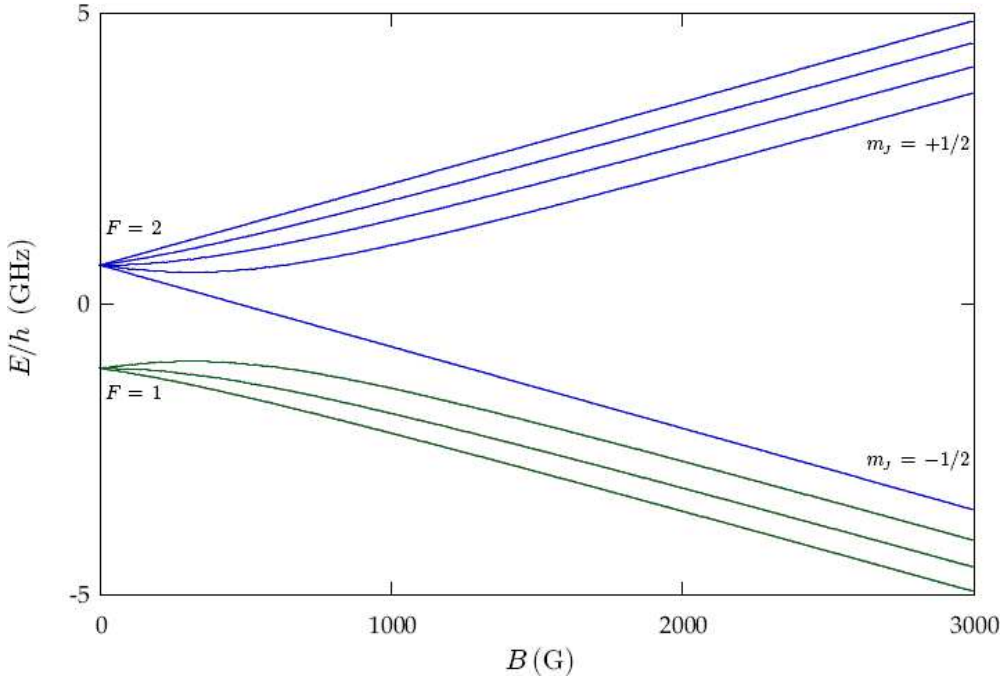

Figure B.4: Sodium $3^2S_{1/2}$ ground state hyperfine structure in an external magnetic field. In the anomalous Zeeman-regime the levels are grouped according to the value of F, in the Paschen-Back-regime according to the value of m_J [20].

B.3 Dipole matrix elements for Sodium

The hyperfine dipole matrix elements for the Sodium D_1 and D_2 line are calculated using the Wigner-Eckart Theorem, see appendix A.

	$m_F = -2$	$m_F = -1$	$m_F = 0$	$m_F = 1$	$m_F = 2$
F′=3	$\sqrt{\frac{1}{60}}$	$\sqrt{\frac{1}{20}}$	$\sqrt{\frac{1}{10}}$	$\sqrt{\frac{1}{6}}$	$\frac{1}{2}$
F′=2	$\sqrt{\frac{1}{24}}$	$\frac{1}{4}$	$\frac{1}{4}$	$\sqrt{\frac{1}{24}}$	
F′=1	$\sqrt{\frac{1}{40}}$	$\sqrt{\frac{1}{80}}$	$\sqrt{\frac{1}{240}}$		

Table B.2: Sodium D_2-line hyperfine dipole transition matrix elements for σ^+ transitions ($F = 2m_F \rightarrow F'm'_F = m_F + 1$) in multiples of $\langle J = \frac{1}{2}||\mu^2||J' = \frac{3}{2}\rangle$

	$m_F = -2$	$m_F = -1$	$m_F = 0$	$m_F = 1$	$m_F = 2$
F′=3	$-\sqrt{\frac{1}{12}}$	$-\sqrt{\frac{2}{15}}$	$-\sqrt{\frac{3}{20}}$	$-\sqrt{\frac{2}{15}}$	$-\sqrt{\frac{1}{12}}$
F′=2	$-\sqrt{\frac{1}{12}}$	$-\sqrt{\frac{1}{48}}$	0	$\sqrt{\frac{1}{48}}$	$\sqrt{\frac{1}{12}}$
F′=1		$\sqrt{\frac{1}{80}}$	$\sqrt{\frac{1}{60}}$	$\sqrt{\frac{1}{80}}$	

Table B.3: Sodium D_2-line hyperfine dipole transition matrix elements for π transitions ($F = 2m_F \rightarrow F'm'_F = m_F$) in multiples of $\langle J = \frac{1}{2}||\mu^2||J' = \frac{3}{2}\rangle$

	$m_F = -2$	$m_F = -1$	$m_F = 0$	$m_F = 1$	$m_F = 2$
F′=3	$\frac{1}{2}$	$\sqrt{\frac{1}{6}}$	$\sqrt{\frac{1}{10}}$	$\sqrt{\frac{1}{20}}$	$\sqrt{\frac{1}{60}}$
F′=2		$-\sqrt{\frac{1}{24}}$	$-\frac{1}{4}$	$-\frac{1}{4}$	$-\sqrt{\frac{1}{24}}$
F′=1			$\sqrt{\frac{1}{240}}$	$\sqrt{\frac{1}{80}}$	$\sqrt{\frac{1}{40}}$

Table B.4: Sodium D_2-line hyperfine dipole transition matrix elements for σ^- transitions ($F = 2m_F \rightarrow F'm'_F = m_F - 1$) in multiples of $\langle J = \frac{1}{2}||\mu^2||J' = \frac{3}{2}\rangle$

	$m_F = -1$	$m_F = 0$	$m_F = 1$
F′=2	$\sqrt{\frac{1}{48}}$	$\frac{1}{4}$	$\sqrt{\frac{1}{8}}$
F′=1	$\sqrt{\frac{5}{48}}$	$\sqrt{\frac{5}{48}}$	
F′=0	$\sqrt{\frac{1}{12}}$		

Table B.5: Sodium D_2-line hyperfine dipole transition matrix elements for σ^+ transitions ($F = 1 m_F \rightarrow F' m'_F = m_F + 1$) in multiples of $\langle J = \frac{1}{2} \| \mu^2 \| J' = \frac{3}{2} \rangle$

	$m_F = -1$	$m_F = 0$	$m_F = 1$
F′=2	$-\frac{1}{4}$	$-\sqrt{\frac{1}{12}}$	$-\frac{1}{4}$
F′=1	$-\sqrt{\frac{5}{48}}$	0	$\sqrt{\frac{5}{48}}$
F′=0		$\sqrt{\frac{1}{12}}$	

Table B.6: Sodium D_2-line hyperfine dipole transition matrix elements for π transitions ($F = 1 m_F \rightarrow F' m'_F = m_F$) in multiples of $\langle J = \frac{1}{2} \| \mu^2 \| J' = \frac{3}{2} \rangle$

	$m_F = -1$	$m_F = 0$	$m_F = 1$
F′=2	$\frac{1}{4}$	$\frac{1}{4}$	$\sqrt{\frac{1}{48}}$
F′=1		$-\sqrt{\frac{5}{48}}$	$-\sqrt{\frac{5}{48}}$
F′=0			$\sqrt{\frac{1}{12}}$

Table B.7: Sodium D_2-line hyperfine dipole transition matrix elements for σ^- transitions ($F = 1 m_F \rightarrow F' m'_F = m_F - 1$) in multiples of $\langle J = \frac{1}{2} \| \mu^2 \| J' = \frac{3}{2} \rangle$

	$m_F = -2$	$m_F = -1$	$m_F = 0$	$m_F = 1$	$m_F = 2$
F′=2	$\sqrt{\frac{1}{12}}$	$\sqrt{\frac{1}{8}}$	$\sqrt{\frac{1}{8}}$	$\sqrt{\frac{1}{12}}$	
F′=1	$\frac{1}{2}$	$\sqrt{\frac{1}{8}}$	$\sqrt{\frac{1}{24}}$		

Table B.8: Sodium D_1-line hyperfine dipole transition matrix elements for σ^+ transitions ($F = 2 m_F \rightarrow F' m'_F = m_F + 1$) in multiples of $\langle J = \frac{1}{2} \| \mu^2 \| J' = \frac{1}{2} \rangle$

	$m_F = -2$	$m_F = -1$	$m_F = 0$	$m_F = 1$	$m_F = 2$
F′=2	$-\sqrt{\frac{1}{6}}$	$-\sqrt{\frac{1}{24}}$	0	$\sqrt{\frac{1}{24}}$	$\sqrt{\frac{1}{6}}$
F′=1		$\sqrt{\frac{1}{8}}$	$\sqrt{\frac{1}{6}}$	$\sqrt{\frac{1}{8}}$	

Table B.9: Sodium D_1-line hyperfine dipole transition matrix elements for π transitions ($F = 2m_F \rightarrow F'm'_F = m_F$) in multiples of $\langle J = \frac{1}{2}||\mu^2||J' = \frac{1}{2}\rangle$

	$m_F = -2$	$m_F = -1$	$m_F = 0$	$m_F = 1$	$m_F = 2$
F′=2		$-\sqrt{\frac{1}{12}}$	$-\sqrt{\frac{1}{8}}$	$-\sqrt{\frac{1}{8}}$	$-\sqrt{\frac{1}{12}}$
F′=1			$\sqrt{\frac{1}{24}}$	$\sqrt{\frac{1}{8}}$	$\frac{1}{2}$

Table B.10: Sodium D_1-line hyperfine dipole transition matrix elements for σ^- transitions ($F = 2m_F \rightarrow F'm'_F = m_F - 1$) in multiples of $\langle J = \frac{1}{2}||\mu^2||J' = \frac{1}{2}\rangle$

	$m_F = -1$	$m_F = 0$	$m_F = 1$
F′=2	$-\sqrt{\frac{1}{24}}$	$-\sqrt{\frac{1}{8}}$	$\frac{1}{2}$
F′=1	$-\sqrt{\frac{1}{24}}$	$-\sqrt{\frac{1}{24}}$	

Table B.11: Sodium D_1-line hyperfine dipole transition matrix elements for σ^+ transitions ($F = 1m_F \rightarrow F'm'_F = m_F + 1$) in multiples of $\langle J = \frac{1}{2}||\mu^2||J' = \frac{1}{2}\rangle$

	$m_F = -1$	$m_F = 0$	$m_F = 1$
F′=2	$\sqrt{\frac{1}{8}}$	$\sqrt{\frac{1}{6}}$	$\sqrt{\frac{1}{8}}$
F′=1	$\sqrt{\frac{1}{24}}$	0	$-\sqrt{\frac{1}{24}}$

Table B.12: Sodium D_1-line hyperfine dipole transition matrix elements for π transitions ($F = 1m_F \rightarrow F'm'_F = m_F$) in multiples of $\langle J = \frac{1}{2}||\mu^2||J' = \frac{1}{2}\rangle$

	$m_F = -1$	$m_F = 0$	$m_F = 1$
F′=2	$-\frac{1}{2}$	$-\sqrt{\frac{1}{8}}$	$-\sqrt{\frac{1}{24}}$
F′=1		$\sqrt{\frac{1}{24}}$	$\sqrt{\frac{1}{24}}$

Table B.13: Sodium D_1-line hyperfine dipole transition matrix elements for σ^- transitions ($F = 1m_F \rightarrow F'm'_F = m_F - 1$) in multiples of $\langle J = \frac{1}{2}||\mu^2||J' = \frac{1}{2}\rangle$

Appendix C

Einstein-coefficients for Rubidium

The values for the Einstein-coefficients used to calculate the magic wavelength in Rubidium are summarized in table C.1 and C.2, together with the respective wavelengths for the observed transition. If experimental data is not available we use dipole transition matrix elements calculated by Safronova et al. [19] to determine the Einstein-coefficients using eq. 2.34.

transition	λ (nm)	source	$A_{ik}(\cdot 10^6 1/s)$	source
$5S_{1/2} \rightarrow 5P_{1/2}$	794.9788509	[34]	36.1285	[34]
$5S_{1/2} \rightarrow 5P_{3/2}$	780.241209686	[34]	38.1156	[34]
$5S_{1/2} \rightarrow 6P_{1/2}$	421.6726	[18]	1.769	[35]
$5S_{1/2} \rightarrow 6P_{3/2}$	420.2989	[18]	1.499	[35]
$5S_{1/2} \rightarrow 7P_{1/2}$	359.2597	[18]	0.2890	[35]
$5S_{1/2} \rightarrow 7P_{3/2}$	358.8073	[18]	8.300	[35]
$5S_{1/2} \rightarrow 8P_{1/2}$	335.1775	[18]	$8.912 \cdot 10^{-2}$	[35]
$5S_{1/2} \rightarrow 8P_{3/2}$	334.9658	[18]	0.1370	[35]
$5S_{1/2} \rightarrow 9P_{1/2}$	323.0088	[18]	$4.231 \cdot 10^{-2}$	[35]
$5S_{1/2} \rightarrow 9P_{3/2}$	322.8911	[18]	$6.380 \cdot 10^{-2}$	[35]
$5S_{1/2} \rightarrow 10P_{1/2}$	315.9173	[18]	$2.209 \cdot 10^{-2}$	[35]
$5S_{1/2} \rightarrow 10P_{3/2}$	315.8444	[18]	$3.716 \cdot 10^{-2}$	[35]
$5S_{1/2} \rightarrow 11P_{1/2}$	311.3950	[18]	$1.398 \cdot 10^{-2}$	[35]
$5S_{1/2} \rightarrow 11P_{3/2}$	311.3468	[18]	$2.763 \cdot 10^{-2}$	[35]
$5S_{1/2} \rightarrow 12P_{1/2}$	308.3229	[18]	$7.692 \cdot 10^{-3}$	[35]
$5S_{1/2} \rightarrow 12P_{3/2}$	308.2893	[18]	$1.639 \cdot 10^{2}$	[35]
$5S_{1/2} \rightarrow 13P_{1/2}$	306.1375	[18]	$4.955 \cdot 10^{-3}$	[35]
$5S_{1/2} \rightarrow 13P_{3/2}$	306.1131	[18]	$1.155 \cdot 10^{-2}$	[35]

Table C.1: Wavelengths and Einstein-coefficients for the calculation of the energy shift of the ground state

transition	λ (nm)	source	$A_{ik}(\cdot 10^6 1/s)$	source
$5P_{3/2} \rightarrow 6S_{1/2}$	1366.875	[18]	14.63	[36]
$5P_{3/2} \rightarrow 7S_{1/2}$	741.02136	[18]	4.552	[19]
$5P_{3/2} \rightarrow 8S_{1/2}$	616.13310	[18]	2.183	[19]
$5P_{3/2} \rightarrow 4D_{3/2}$	1529.261	[18]	1.776	[19]
$5P_{3/2} \rightarrow 4D_{5/2}$	1529.366	[18]	10.67	[19]
$5P_{3/2} \rightarrow 5D_{3/2}$	776.15716	[18]	0.6711	[19]
$5P_{3/2} \rightarrow 5D_{5/2}$	775.97855	[18]	3.937	[19]
$5P_{3/2} \rightarrow 6D_{3/2}$	630.09666	[18]	0.6305	[19]
$5P_{3/2} \rightarrow 6D_{5/2}$	630.00670	[18]	3.717	[19]

Table C.2: Wavelengths and Einstein-coefficients for the calculation of the energy shift of the $5P_{3/2}$ state

Bibliography

[1] J. V. Prodan, W. D. Phillips, H. Metcalf, Laser Production of a very slow monoenergetic atomic beam, Phys. Rev. Lett. **49**, 1149 (1982)

[2] S. Chu, L. Hollberg, J. E. Bjorkholm, A. Cable, A. Ashkin, Three-dimensional viscous confinement and cooling of atoms by resonance radiation pressure, Phys. Rev. Lett. **55**, 48 (1985)

[3] M. H. Anderson, J. R. Ensher, M. R. Matthews, C. E. Wieman, E. A. Cornell, Observation of Bose-Einstein Condensation in a Dilute Atomic Vapor, Science **268**, 198 (1995)

[4] A. Einstein, Sitz. Ber. Preuss. Akad. Wiss. (Berlin) 1, 3 (1925)

[5] M. Greiner, O. Mandel, T. Esslinger, T. W. Hänsch, I. Bloch, Quantum phase transition from a superfluid to a Mott insulator in a gas of cold atoms, Nature **415**, 39 (2002)

[6] C. Cohen-Tannoudji, B. Diu, F. Laloe, Quantum Mechanics Vol. II, Wiley (1977)

[7] B. H. Bransden, C. J. Joachin, Physics of Atoms and Molecules, Prentice Hall (2003)

[8] H. J. Metcalf, P. van der Straten, Laser cooling and trapping, Springer-Verlag (1999)

[9] L. Allen, J. H. Eberly, Optical resonance and two-level atoms, Wiley (1975)

[10] R. Loudon, The quantum theory of light, Clarendon Press (1983)

[11] C. Degenhardt, H. Stoehr, U. Sterr, F. Riehle, C. Lisdat, Wavelength-dependat ac Stark shift of the $^1S_0 - ^3P_1$ transition at 657nm in Ca, Phys. Rev. A **70**, 023414 (2004)

[12] R. N. Zare, Angular Momentum, Wiley (1988)

[13] C. S. Adams, S. G. Cox, E. Riis, A. S. Arnold, Laser cooling in a 'golden ratio' quasi-ectrostatic lattice, Jour. Phys. B **36**, 1933 (2003)

[14] D. M. Meekhof, S. R. Jefferts, M. Stepanovic, T. E. Parker, Accuracy evaluation of a cesium fountain primary frequency standard at NIST, IEEE **50**, 507 (2001)

[15] M. Takamoto, F.-L. Hong, R. Higashi, H. Katori, An optical lattice clock, Nature **435**, 321 (2005)

[16] C.-S. Chuu, F. Schreck, T. P. Meyrath, J. L. Hanssen, G. N. Price, M. G. Raizen, Direct observation of Sub-Poissonian Number Statistics in a Degenerate Bose Gas, Phys. Rev. Lett. **95**, 260403 (2005)

[17] M. Takamoto, H. Katori, Spectroscopy of the $^1S_0 - ^3P_0$ Clock Transition of ^{87}Sr in an optical lattice, Phys. Rev. Lett. **91**, 223001 (2003)

[18] http://physics.nist.gov

[19] M. S. Safronova, C. J. Williams, C. W. Clark, Relativistic many-body calculations of electric dipole moments, lifetimes, and polarizabilities in rubidium, Phys. Rev. A **69**, 022509 (2004)

[20] D. Steck, Sodium D line data, http://steck.us/alkalidata

[21] B. Gutierrez-Medina, Quantum Transport and Control of Atomic Motion with Light, Ph.D. Thesis (2004)

[22] J. E. Thomas, Uncertainty-limited position measurement of moving atoms using optical fields, Opt. Lett. **14**, 1186 (1989)

[23] M. Kasevich, D. S. Weiss, E. Riis, K. Moler, S. Kasapi, S. Chu, Atomic Velocity Selection Using Stimulated Raman Transitions, Phys. Rev. Lett. **66**, 2297, (1991)

[24] K. D. Stokes, C. Schnurr, J. R. Gardner, M. Marable, G. R. Welch, J. E. Thomas, Precision Position Measurement of Moving Atoms Using Optical Fields, Phys. Rev. Lett. **67**, 1997 (1991)

[25] J. R. Gardner, M. L. Marable, G. R. Welch, J. E. Thomas, Suboptical Wavelength Position Measurement of Moving Atoms Using Optical Fields, Phys. Rev. Lett. **70**, 3404 (1993)

[26] S. M. Barnett, P. M. Radmore, Methods in Theoretical Quantum Optics, Oxford Science Publications (1997)

[27] P. R. Hemmer, G. P. Ontai, S. Ezekiel, Precision studies of stimulated-resonance Raman interactions in an atomic beam, J. Opt. Soc. Am. B **3**, 219 (1986)

[28] K. Moler, D. S. Weiss, M. Kasevich, S. Chu, Theoretical analysis of velocity-selective Raman transitions, Phys. Rev. A **45**, 342 (1992)

[29] T. A. Savard, Raman Induced Resonance Imaging of trapped atoms, Ph.D. Thesis (1998)

[30] T. A. Savard, S. R. Grande, K. M. O'Hara, M. E. Gehm, J. E. Thomas, Raman-induced magnetic resonance imaging of atoms in a magneto-optical trap, Phys. Rev. A **60**, 4788, (1999)

[31] K. B. Davis, M.-O. Mewes, M. R. Andrews, N. J. van Druten, D. S. Durfee, D. M. Kurn, W. Ketterle, Bose-Einstein Condensation in a Gas of Sodium Atoms, Phys. Rev. Lett. **75**, 3969 (1995)

[32] A. R. Edmonds, Angular Momentum in quantum mechanics, Princeton (1957)

[33] D. M. Brink, G. R. Satchler, Angular Momentum, Oxford University Press (1962)

[34] D. Steck, Rubidium D Line Data, http://steck.us/alkalidata

[35] D. C. Morton, Atomic Data for Resonant Absorption Lines. II. Wavelengths Longward of the Lyman Limit for Heavy Elements, Astrophys. J. Supp. Ser. **130**, 403 (2000)

[36] E. Gomez, F. Baumer, A. D. Lange, G. D. Sprouse, L. A. Orozco, Lifetime measurement of the 6s level of Rubidium, Phys. Rev. A **72**, 012502 (2005)